Goddard High Resolution Spectrograph Science Verification
and Data Analysis

FINAL REPORT
Contract NAS5-31218
29 January 1992

Prepared by:
Advanced Computer Concepts, Inc.
11518 Gainsborough Road
Potomac, Maryland 20854

Prepared for:
National Aeronautics and Space Administration
Goddard Space Flight Center
Greenbelt, Maryland 20771

CONTENTS

This report summarizes the results of the work performed by Advanced Computer Concepts, Inc. under Contract NAS5-31218 with the National Aeronautics and Space Administration Goddard Space Flight Center titled "GHRS Science Verification Data Analysis."

1. CALIBRATION SUPPORT FOR THE GHRS.

The majority of the data analysis we performed to support the Orbital Verification (OV) and Science Verification (SV) of the Goddard High Resolution Spectrograph (GHRS) was in the areas of the Digicon detector's performance and stability, wavelength calibration, and geomagnetic induced image motion. The following sections briefly describe the results of the analyses. Detailed results can be found in the attachments.

1.1 Digicon Performance and Stability.

The geometric transformation which relates the Digicon's X and Y deflections and the diode position to a position on the photocathode is modeled by the equations in Attachment 1. We computed the coefficients of this model using both pre-launch calibration data taken in 1984 and post-launch data taken during OV and SV. Our analysis showed no significant changes with time (Attachment 1 and 2). This indicates that any aging effects in the Digicon's permanent magnet is minimal.

A detector stability minifunctional was run 10 times for both GHRS detectors during the period of November 12, 1990 through June 9, 1991. Our results show no changes in the focus or the geometric properties of the detectors over the 7 month period. The deflection step size remained stable to within 1 percent and the dark count remained at approximately 0.01 counts second/diode for both detectors. The only significant change was a decrease in the observed flat field lamp count rate. The count rate is decreasing at a rate of approximately 7 percent per year. It has not yet been determined whether this decrease is a result of a detector sensitivity loss or a decrease in the light output of the flat field lamps. Simular decreases were found in the data from the wavelength calibration lamps which would indicate that a loss of detector sensitivity is the most likely explanation. More detailed discussion of the detector stability can be found in Attachment 2.

1.2 Geomagnetic Induced Image Motion.

We have found that the GHRS detectors are susceptible to geomagnetically induced image motion from analysis of OV/SV spectral calibration lamp data and target acquisition deflection calibration data. We have measured the motion due to the Earth's magnetic field

and found that the motion at the diode array is approximately 10 microns (0.2 diodes/Gauss) for detector 1 and 50 microns (1.0 diode Gauss) for detector 2. This motion can cause errors in target acquisition, errors in measured wavelengths, and can result in a loss of spectral resolution. The impact of the magnetically induced motion can be minimized by limiting spectral observations to less than 5 minutes and by using the double located mode of target acquisition. Detailed results of the magnetic motion problem can be found in attachment 3.

1.3 OV SV Wavelength Calibration.

We have analyzed the GHRS OV SV spectral calibration lamp observations and have found that an average dispersion coefficient table with linear thermal motion models can be used to compute wavelengths for science observations with the target in the small science aperture (SSA) to better than one photocathode sample unit (50 microns). We have found that the majority of the spectral image motion can be modeled as a linear function of the temperature. Selection of the best thermistor to use in the model varies with grating mode. Gratings 3 and 4, with a motion range of 300 microns, are most susceptible to thermal motion. In addition to the thermal motion, we have observed plate scale variations on the order of 0.1 percent which may also be thermally induced. Details of this analysis can be found in attachment 4.

We have made measurements of the spectral offsets between the large (LSA) and small science apertures for GHRS gratings 2, 3, and 4. In all cases the measured offsets were less than one diode and the average for each grating was less than 1/2 didoe. There was insufficient data to quantify changes in the offsets for varing carrousel and photocathode sample positions. However, our results for grating 2 indicate that the offset does vary with carrousel position. More detailed analysis of the LSA to SSA offsets can be found in attachment 5.

2.0 SOFTWARE DEVELOPMENT

Another major task in our support of GHRS OV SV data analysis was to provide software developemnt and maintainance support for the GHRS data management and analysis system. This system is installed on the GHRS Vax at NASA/Goddard Space Flight Center running under the VMS operating system. A significant portion of the software was also converted to run under both UNIX and MS-DOS operating systems. The software is written almost exclusively in Interactive Data Language (IDL).

We have continued the conversion of the GHRS software from IDL version

1 to IDL version 2. The major reason for this conversion is that IDL version 1 only runs on a VAX VMS machine. Conversion to version 2 allows use of the software under VMS, UNIX and MS-DOS machines. Although only minor changes in most of the software was required to convert to IDL version 2 a significant amount of effort was required to convert internal binary data sets from one machine to another. We have written routines to convert the three most popular data formats used by the GHRS software system from the VAX to other machines. These formats include the Science Data Analysis System (SDAS) image and table formats and the GHRS data base format.

3.0 GHRS CALIBRATION REFERENCE FILES.

We formatted the following calibration files computed by the GHRS team according to the specifications in the Space Telescope Science Institute (ST ScI) document "Hubble Space Telescope Spectrograph Calibration Data Specifications." We delivered the to the ST ScI for use the the routine data processing of GHRS data.

FILE	Description	Delivery Date
DC_002.TAB	Average OV SV wavelength dispersion coefficients. They do not include a thermal motion model.	June 10, 1991
IA_001.TAB	Incidence angle corrections for computing the wavelength offset between the small science aperture and the spectral calibration lamp apertures.	June 10, 1991
SMAP_002.TAB	Average photocathode sample mapping function coefficients.	June 10, 1991
VG_G1_01.HH* VG_G2_02.HH* VG_G3_01.HH* VG_G4_01.HH* VG_G5_01.HH*	Files containing the vignetting curves for the first order gratings.	June 10, 1991
DIO_D1_1.HH* DIO_D2_1.HH*	Contains the diode response computed from internal flat field lamp observations.	June 10, 1991
SF_G1_01.HH* SF_G2_01.HH* SF_G3_01.HH* SF_G4_01.HH* SF_G5_01.HH*	Contains the sensitivity curves for each of the first order gratings.	June 10, 1991

WF_G1_01.HH* WF_G2_01.HH* WF_G3_01.HH* WF_G4_01.HH* WF_G5_01.HH*	Contains the wavelength vectors for the above sensitivity curves.	June 10, 1991
DC_004.TAB	New average wavelength dispersion coefficients which include provisions for a thermal motion model.	Sept. 6, 1991
TM_002.TAB	Coefficients for thermal spectral motion.	Sept. 6, 1991
IA_001.TAB	Incidence angle coefficients tabulated with new grating names. Actual coefficients are unchanged.	Sept. 6, 1991
SMAP_003.TAB	Final SV average sample mapping coefficients.	Sept. 6, 1991
VG_G1_02.HH* VG_G2_03.HH* VG_G3_02.HH* VG_G4_02.HH* VG_G5_02.HH*	Update of previous files. These files are constructed so that interpolation between curves is done using the photocathode line position instead of carrousel position	Sept. 6, 1991
WF_G1_01.HH* WF_G2_01.HH* WF_G3_01.HH* WF_G4_01.HH* WF_G5_01.HH* SF_G1_01.HH* SF_G2_01.HH* SF_G3_01.HH* SF_G4_01.HH* SF_G5_01.HH*	Redelivery of the first order grating sensitivity curves using the new grating names.	Sept. 6, 1991
WF_EA_01.HH* SF_EA_01.HH* WF_EB_01.HH* WF_EB_01.HH*	Sensitivity curves for the echelle grating modes.	Sept. 6, 1991
CCRA_2.TAB CCR9_2.TAB	Tables containing improved echelle B ripple coefficients computed from prelaunch miniarc lamp data.	Oct. 30, 1991
IA_002.TAB	Contains the incidence angle coefficients for gratings 2, 3 and 4	Oct. 30, 1991

large science aperture data.

CCR3_1.TAB   Table of detector parameters which   Dec. 1, 1991
                 contain the order of the new
                 background fitting polynomial.

CCRB.TAB   Echelle scattered light coefficient   Dec. 1, 1991
   table.

4.0 RESTORATION OF IRAS LARGE MAGELLANIC CLOUD DATA.

We have continued the restoration of the IRAS Additional Observations (AO) of the Large Magellanic Cloud (LMC) using the blocked iterative restoration algorithm described in attachment C. Our restoration algorithm works with the raw data scans without regridding or interpolating the data on an equally spaced image grid. To do this, we must use a different point spread function for each scan angle, direction and detector.

Results of the restorations of the 30 Doradus region of the LMC are shown in figure 1 for each of the 4 IRAS wavelength bands. The images on the left show the results of regridding the raw data without attempting any deconvolution. The images on the right show the deconvolution results. Figure 2 shows the deconvolution of the entire data set for the 60 micron wavelength band.
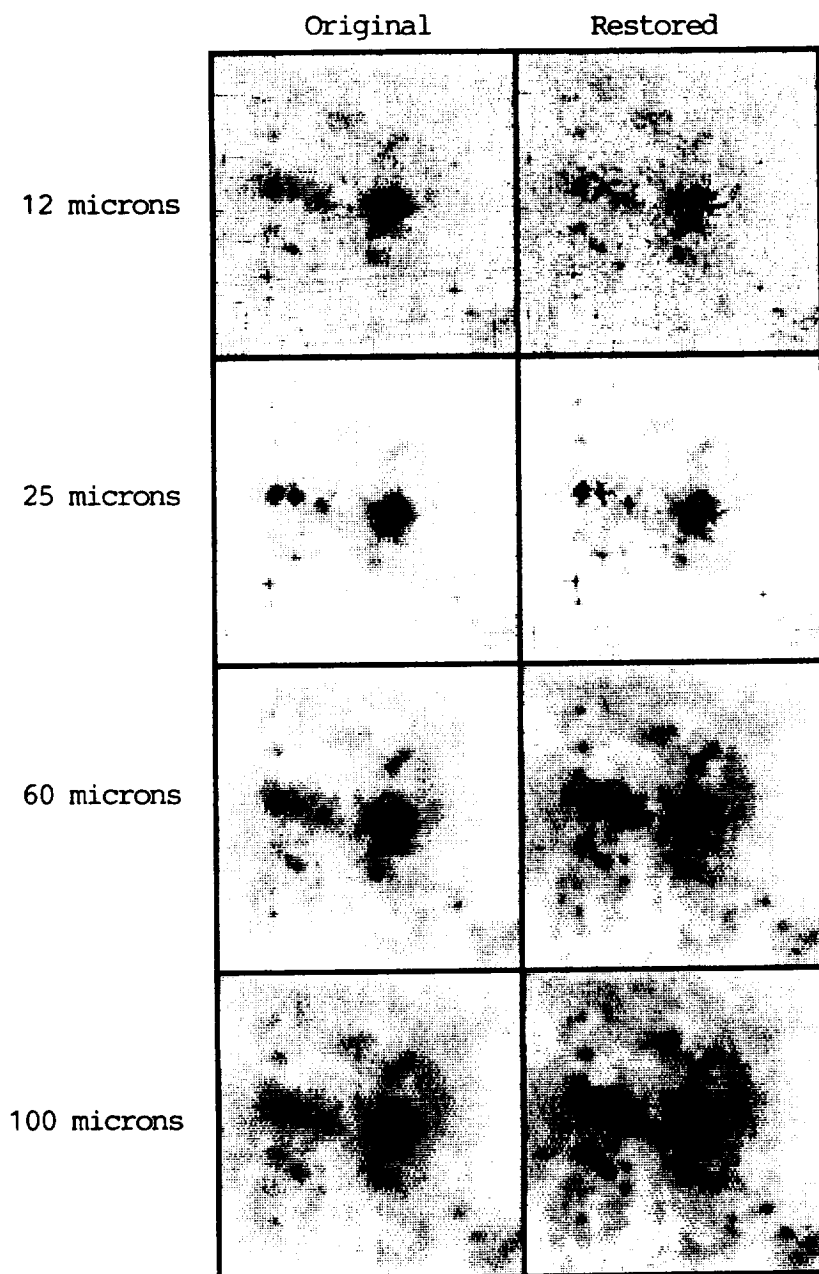
FIGURE 2
Restoration of the 60 micron IRAS AO data
of the Large Magellanic Clouds
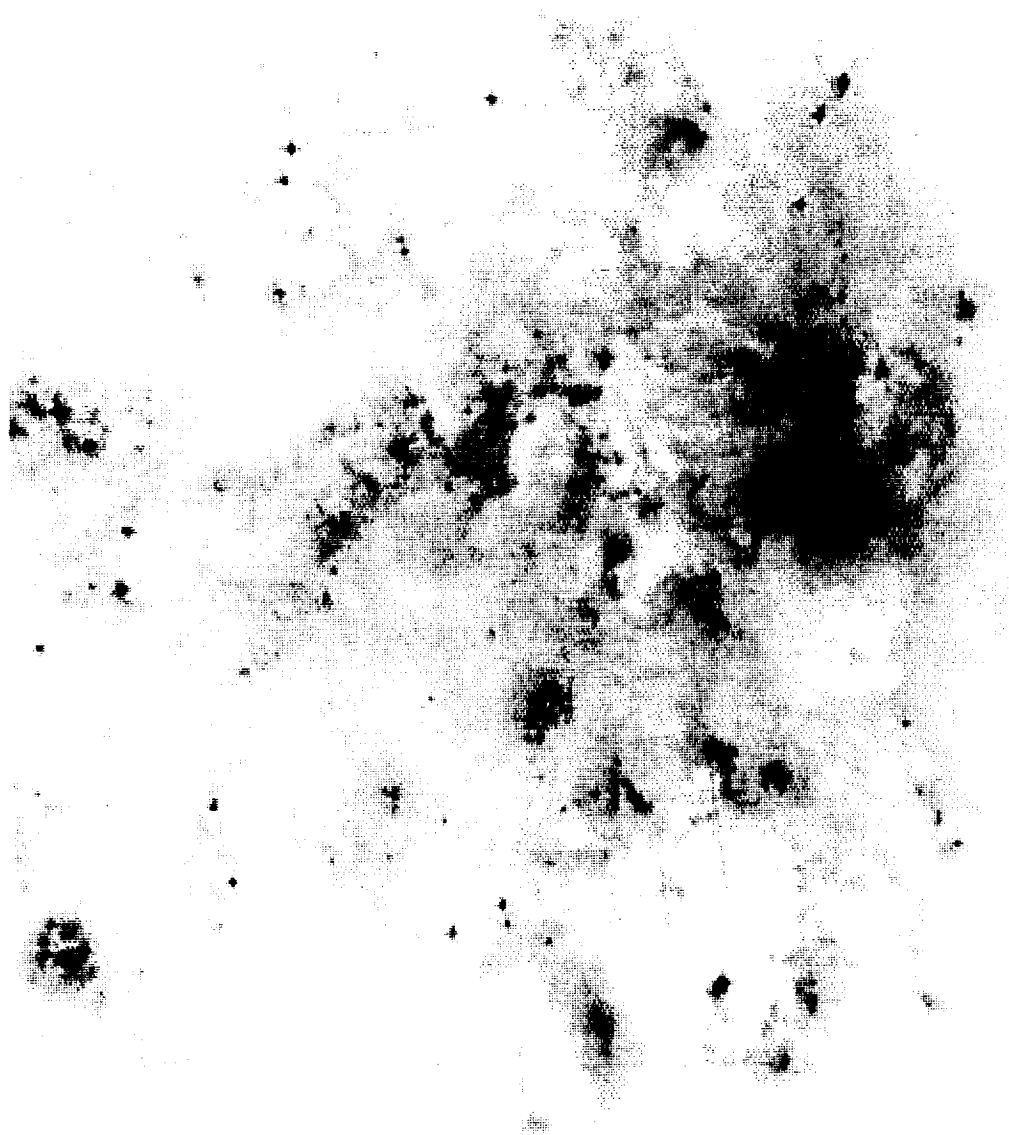
FIGURE 1
Restoration of the 30 Doradus
Region of the LMC

GHRS PHOTOCATHODE MAPPING FUNCTION

D.J. Lindler
11 July 1991

ABSTRACT

The post-launch GHRS photocathode mapping function which relates
digicon deflections and diode positions to photocathode line and
sample positions show no significant change from pre-launch
computations. This indicates that any aging effects in the permanent
magnet or the digicon is minimal. Observations over an 8 month period
after launch also show no significant changes with time. This report
describes the post-launch calibration. Tables of the resulting
coefficients are presented.

1. INTRODUCTION

The GHRS phocathode line and sample mapping functions which relate
digicon deflection and diode number to photocathode line and sample
positions are given by:

$$L = L0 + A*dy$$
$$S = S0 + B*dx + E*D$$

where,

  L is the line postion in 50 micron sample units
    defined so that the upper photocathode mask edge
    is at position 0.0.
  S is the sample position in 50 micron sample units
    defined so that the left photocathode mask edge
    is at position 0.0.
  dy is the y-deflection minus 2048.
  dx is the x-deflection minus 2048.
  D is the diode position starting at 0 for the first
    diode on the main diode array.
  L0 and A are cofficients which vary by detector.
  S0, B, and E are coefficients which vary by detector
    and y-deflection.

L0 and S0 give the photocathode line and sample position which the
first diode observes at null x and y defelctions (2048, 2048). A and
B give the deflection step size as a fraction of 50 micron sample
units. E gives the separation of the position on the photocathode
viewed by neighboring diodes.

These coefficients are computed using observations of the four photocathode mask edges illuminated by a flat field lamp. L0 and A are computed from the y-deflections which center the diode array on the top (YTOP) and bottom (YBOTTOM) photocathode mask edge.

$$A = 430.0 / (YBOTTOM - YTOP)$$

$$L0 = (2048 - YTOP) * A$$

The coefficients S0, B, and E are computed from observations of the left and right photocathode masks edges observed at various x-deflections. The diode positions of the edge are tabulated versus x-deflection. The sample mapping coefficients are then computed from the table values by a least squares fit.

2. DATA REDUCTION

The line mapping function coefficients were computed using the routine MAPLCAL on the observations in table 1. MAPLCAL was called using all default parameters by;

        LMAPCAL,[ID1, ID2], 0, TABLE

where ID1 and ID2 are the observation entry numbers for the top and bottom edge observations. The coefficients are written into an SDAS table file specfied by TABLE. LMAPCAL was run on each pair of top and bottom edge locations listed in table 1. For example, the first pair of observations were calibrated using;

        LMAPCAL, [34, 35], 0, 'table1'

The sample mapping function coefficients were computed using the routine MAPSCAL on the observations in table 2. MAPSCAL was called using all default parameters by;

        SMAPCAL, ID, 0, TABLE

where ID is the observation entry number and TABLE is the output SDAS table file name where the output coefficients are tabulated versus y-deflection.

3. RESULTS

Table 3 shows the tabulated line mapping function for each pair of top and bottom edge scans and table 4 shows an average of the results. Small changes in L0 can be attributed to statistical errors in the measurements and to geomagnetic image motion. The deflection step

size vaule, A, is stable to 1 percent. Small changes in this value can be attributed to statistical errors in the measurements, small fluctuations in the photocathode high voltage, differential magnetic field vectors between the top and bottom edge observations, and possible small thermal effects. Table 4 also shows the average value of the coefficients computed during the GHRS phase 6 calibration in 1984. The small changes since 1984 may be the result of adjustments to the photocathode high voltage to improve detector focus and digicon aging over seven years.

Table 5 shows the sample mapping function coefficients for each of the observations in table 2 tabulated versus detector and y-deflection. Table 6 shows the averages over the observations. The deflection step size, B, is within 1 percent of the nominal 1/8 diode value (0.125) needed to insure that combaddition does not degrade spectral resolution. Table 6 also shows that the deflection step size is stable to within approximately one percent. Changes in the coefficients can be attributed to statistical errors in the measurements, small fluctuations in the photocathode high voltage, geomagnetic image motion, and possible small thermal effects. Again the small deviations from the 1984 coefficients shown in table 7 can be attributed to adjustments in the photocathode voltage and possible digicon aging.

TABLE 1
Line Mapping Function Observations

ENTRY	ROOTNAME	DET	START_TIME	Photocathode Edge
34	Z06H0609T	1	16-JUN-1990 06:52	Top
35	Z06H060AT	1	16-JUN-1990 07:02	Bottom
135	Z06H5609T	1	24-JUL-1990 10:44	Top
136	Z06H560AT	1	24-JUL-1990 10:54	Bottom
565	Z06H6609T	1	10-SEP-1990 12:01	Top
566	Z06H660AT	1	10-SEP-1990 12:11	Bottom
907	Z0E90N03T	1	21-NOV-1990 01:32	Top
908	Z0E90N04T	1	21-NOV-1990 01:41	Bottom
61	Z06H0709T	2	18-JUN-1990 06:27	Top
62	Z06H070AT	2	18-JUN-1990 06:37	Bottom
239	Z06H5709T	2	24-JUL-1990 14:09	Top
240	Z06H570AT	2	24-JUL-1990 14:18	Bottom
575	Z06H6709T	2	10-SEP-1990 15:26	Top
576	Z06H670AT	2	10-SEP-1990 15:35	Bottom

TABLE 2
Sample Mapping Function Observations

ENTRY	ROOTNAME	DETECTOR	START_TIME
33	Z06H0608T	1	16-JUN-1990 06:44
276	Z06H5608T	1	24-JUL-1990 10:36
564	Z06H6608T	1	10-SEP-1990 11:53
906	Z0E90N02T	1	21-NOV-1990 01:24
60	Z06H0708T	2	18-JUN-1990 06:19
238	Z06H5708T	2	24-JUL-1990 14:00
574	Z06H6708T	2	10-SEP-1990 15:17

TABLE 3
GHRS Line Mapping Function Coefficients

Detector	date	ID1	L0	A	YTOP	YBOTTOM
1	16-JUN-1990	34	214.17	0.1262	350.5	3758.6
1	24-JUL-1990	135	214.27	0.1262	349.7	3757.9
1	10-SEP-1990	565	214.14	0.1261	349.9	3759.8
1	21-NOV-1990	907	214.24	0.1263	351.3	3756.7
2	18-JUN-1990	61	225.13	0.1240	232.7	3700.0
2	24-JUL-1990	239	225.10	0.1239	231.2	3701.8
2	10-SEP-1990	575	225.31	0.1241	232.0	3697.8

TABLE 4
Average Line Mapping Function Coefficients

Detector	L0	RMS(L0)	A	RMS(A)	L0(1984)	A(1984)
1	214.21	0.06	0.1262	0.0001	213.56	0.1267
2	225.18	0.12	0.1240	0.0001	224.84	0.1245

TABLE 5
GHRS Sample Mapping Function Coefficients

Detector	date	ID	YDEF	S0	B	E
1	16-JUN-1990	33	500	30.17	0.1260	1.00161
1	24-JUL-1990	276	500	29.99	0.1259	1.00179
1	10-SEP-1990	564	500	30.16	0.1259	1.00166
1	21-NOV-1990	906	500	30.20	0.1260	1.00168
1	16-JUN-1990	33	1000	30.68	0.1259	1.00192
1	24-JUL-1990	276	1000	30.52	0.1257	1.00209
1	10-SEP-1990	564	1000	30.69	0.1258	1.00202
1	21-NOV-1990	906	1000	30.71	0.1259	1.00211
1	16-JUN-1990	33	1500	31.04	0.1256	1.00218
1	24-JUL-1990	276	1500	31.09	0.1257	1.00182
1	10-SEP-1990	564	1500	31.20	0.1258	1.00187
1	21-NOV-1990	906	1500	31.15	0.1258	1.00211
1	16-JUN-1990	33	2000	31.41	0.1257	1.00224
1	24-JUL-1990	276	2000	31.39	0.1255	1.00231
1	10-SEP-1990	564	2000	31.51	0.1256	1.00227
1	21-NOV-1990	906	2000	31.50	0.1257	1.00229
1	16-JUN-1990	33	2500	32.05	0.1258	1.00169
1	24-JUL-1990	276	2500	31.99	0.1256	1.00195
1	10-SEP-1990	564	2500	32.10	0.1257	1.00188
1	21-NOV-1990	906	2500	32.04	0.1257	1.00204
1	16-JUN-1990	33	3000	32.53	0.1255	1.00228
1	24-JUL-1990	276	3000	32.56	0.1254	1.00236
1	10-SEP-1990	564	3000	32.67	0.1255	1.00226
1	21-NOV-1990	906	3000	32.57	0.1256	1.00245
2	18-JUN-1990	60	1000	28.95	0.1249	1.00445
2	24-JUL-1990	238	1000	29.02	0.1249	1.00443
2	10-SEP-1990	574	1000	28.76	0.1248	1.00457
2	18-JUN-1990	60	1500	28.98	0.1246	1.00295
2	24-JUL-1990	238	1500	28.97	0.1245	1.00314
2	10-SEP-1990	574	1500	28.88	0.1247	1.00274
2	18-JUN-1990	60	2000	28.80	0.1241	1.00255
2	24-JUL-1990	238	2000	28.89	0.1242	1.00240
2	10-SEP-1990	574	2000	28.72	0.1243	1.00229
2	18-JUN-1990	60	2500	28.73	0.1241	1.00238
2	24-JUL-1990	238	2500	28.77	0.1241	1.00237
2	10-SEP-1990	574	2500	28.62	0.1242	1.00232
2	18-JUN-1990	60	3000	28.68	0.1243	1.00197
2	24-JUL-1990	238	3000	28.72	0.1243	1.00192
2	10-SEP-1990	574	3000	28.56	0.1244	1.00200
2	18-JUN-1990	60	3500	28.91	0.1242	0.99983
2	24-JUL-1990	238	3500	28.93	0.1241	0.99983
2	10-SEP-1990	574	3500	28.84	0.1243	0.99975

TABLE 6
Average Sample Mapping Function Coefficients

DETECTOR	YDEF	S0	RMS(S0)	B	RMS(B)	E	RMS(E)
1	500	30.13	0.09	0.1260	0.0001	1.0017	0.0001
1	1000	30.65	0.09	0.1258	0.0001	1.0020	0.0001
1	1500	31.12	0.07	0.1257	0.0001	1.0020	0.0002
1	2000	31.45	0.06	0.1256	0.0001	1.0023	0.0001
1	2500	32.05	0.05	0.1257	0.0001	1.0019	0.0001
1	3000	32.58	0.06	0.1255	0.0001	1.0023	0.0001
2	1000	28.91	0.13	0.1249	0.0001	1.0045	0.0001
2	1500	28.94	0.05	0.1246	0.0001	1.0029	0.0002
2	2000	28.80	0.08	0.1242	0.0001	1.0024	0.0001
2	2500	28.71	0.08	0.1241	0.0001	1.0024	0.0001
2	3000	28.65	0.08	0.1243	0.0001	1.0020	0.0001
2	3500	28.90	0.05	0.1242	0.0001	0.9998	0.0001

TABLE 7
Prelaunch (1984) Sample Mapping Function Coefficients

DETECTOR	YDEF	S0	B	E
1	500	30.94	0.1264	1.0018
1	1000	31.32	0.1262	1.0020
1	1500	31.57	0.1262	1.0022
1	2000	31.84	0.1263	1.0020
1	2500	32.25	0.1264	1.0015
1	3000	32.80	0.1264	1.0010
2	1000	28.58	0.1253	1.0045
2	1500	28.78	0.1251	1.0028
2	2000	28.75	0.1249	1.0023
2	2500	28.80	0.1248	1.0020
2	3000	28.83	0.1249	1.0018
2	3500	29.25	0.1248	0.9994

Analysis of the GHRS Detector
Stability Minifunctionals

D.J. Lindler
July 15, 1991

ABSTRACT

The detector stability minifunctional was run 10 times for both GHRS detectors during the period of November 12, 1990 through June 9, 1991. Results show no changes in the focus or the geometric properties of the detectors over the 7 month period. The deflection step size remained stable to within 1 percent and the dark count remained at approximately 0.01 counts/second/diode for both detectors. The only significant change was a decrease of observed flat field lamp count rate. The count rate is decreasing a rate of approximately 7 percent per year. It has not yet been determined whether this decrease is a result of a detector sensitivity loss or a decrease in the light output of the lamps.

1. INTRODUCTION

The stability minifunctional (proposal 2924) consists of internal detector observations including:

1) A 70 second dark count observation
2) An observation of central region of the photocathode illuminated by the flat field lamp.
3) A focus check consisting of 231 observations at the photocathode mask edge at y-deflection 2048 and varying x-deflections.
4) Left and right photocathode edge scans at y-deflection 2048 for the sample mapping function coefficient computation.
5) Top and bottom photocathode mask edge scans for the line mapping function computation.

2. DARK COUNT MONITORING

The 70 second dark count observation is used to monitor any significant increases in the dark rate and find any diodes which become excessively noisy. The average dark rates in counts/second/diode (c/s/d) over the seven month period are shown in tables 1 and 2. Both detectors remained at approximately the 0.01 c/s/d level with the detector 1 having a slightly lower level than detector 2. None of the observations showed any anomalous noise

events or diodes.

3. DETECTOR FOCUS

Tables 1 and 2 show the detector focus of the seven month period. The focus value tabulated is the full-width-half-maximum of a Gaussian fit to the differential edge profile as computed by routine FOCUS_COMP. It is given in deflections units (1 deflection unit = 6.25 microns). The focus for both detectors has remained stable over the seven month period.

4. FLAT FIELD LAMP

The total flat field count rates in seven substep bins observing the central region of the photocathode are tabulated in tables 1 and 2. Normalized plots of the count rates versus time are shown in figures 1 and 2. Both detectors show the count rate decreasing with time at a rate of approximately 7 percent per year. From this data it can not be deduced whether the detector sensitivity is decreasing or the lamp output is decreasing. The same type of analysis using spectral calibration lamp data show a similar decrease. Figures 3 through 7 show the decrease in the observed count rate for the first order spectral calibration lamp minifunctionals. Different plotting symbols are used to show different carrousel positions.

5. PHOTOCATHODE MAPPING FUNCTION

Tables 3 and 4 show the photocathode mapping functions coefficients computed from the detector minifunctionals. Results indicate that the deflections stepsizes (coefficients A and B) are stable to better than one percent. No time variations in the coefficients are evident.

Table 1
Detector 1 Stability

Date	Focus (def. units)	Average Flat Field	Dark Rate (c/s/d)
12-Nov-90	6.71	4122	.009
01-Dec-90	6.70	4110	.006
15-Dec-90	6.62	4085	.008
14-Jan-91	6.60	4070	.006
25-Jan-91	6.66	4063	.005
15-Feb-91	6.68	4064	.007
28-Feb-91	6.56	4052	.013
12-Mar-91	6.64	4033	.007
28-Mar-91	6.63	4011	.004
09-Jun-91			.006

Table 2
Detector 2 Stability

Date	Focus (def. units)	Average Flat Field	Dark Rate (c/s/d)
12-Nov-90	6.56	1324	0.010
26-Nov-90	6.57	1325	0.010
10-Dec-90	6.55	1317	0.009
17-Jan-91	6.52	1311	0.015
23-Jan-91	6.38	1309	0.013
13-Feb-91	6.42	1306	0.009
28-Feb-91	6.36	1303	0.008
12-Mar-91	6.60	1303	0.007
29-Mar-91	6.56	1301	0.009
09-Jun-91	6.45	1278	0.010

Table 3
Detector Minifunctional - Line Mapping Function

DET	date	ID	ROOTNAME	L0	A	YUPPER	YLOWER
1	12-NOV-1990	880	Z0E90108T	213.98	0.1259	348.2	3764.0
1	2-DEC-1990	1125	Z0E90208T	214.02	0.1262	351.9	3759.6
1	15-DEC-1990	1200	Z0E90308T	214.06	0.1261	349.9	3761.0
1	14-JAN-1991	1552	Z0E90408T	213.95	0.1259	349.3	3763.4
1	25-JAN-1991	1701	Z0E90608T	214.04	0.1262	352.0	3759.3
1	15-FEB-1991	2429	Z0E90508T	214.10	0.1265	355.9	3754.4
1	28-FEB-1991	2844	Z0E90708M	214.04	0.1262	351.9	3759.3
1	12-MAR-1991	2956	Z0E90808T	213.97	0.1258	347.6	3764.9
1	28-MAR-1991	3400	Z0E90908T	213.99	0.1261	351.2	3760.8
1	9-JUN-1991	4103	Z0E90B08M	213.85	0.1263	355.0	3759.3
2	12-NOV-1990	891	Z0E90C08T	224.59	0.1237	232.2	3708.7
2	26-NOV-1990	1028	Z0E90D08T	224.63	0.1237	231.7	3708.5
2	10-DEC-1990	1158	Z0E90E08T	224.60	0.1237	231.8	3708.9
2	17-JAN-1991	1630	Z0E90F08T	224.83	0.1237	230.4	3706.6
2	23-JAN-1991	1690	Z0E90H08T	224.68	0.1237	232.4	3707.2
2	13-FEB-1991	2336	Z0E90G08T	224.89	0.1238	232.0	3704.3
2	28-FEB-1991	2855	Z0E90I08M	224.84	0.1240	235.4	3701.9
2	12-MAR-1991	2945	Z0E90J08T	224.81	0.1237	231.1	3706.4
2	29-MAR-1991	3464	Z0E90K08T	224.84	0.1237	231.0	3705.9
2	9-JUN-1991	4114	Z0E90M08T	224.72	0.1240	236.4	3702.9

Table 4
Detector Minifunctional - Sample Mapping Function

DET	date	ID1	ROOTNAME	YDEF	S0	B	E
1	12-NOV-1990	876	Z0E90104T	2048	31.51	0.1257	1.00147
1	2-DEC-1990	1121	Z0E90204T	2048	31.82	0.1259	1.00074
1	15-DEC-1990	1196	Z0E90304T	2048	31.62	0.1257	1.00145
1	14-JAN-1991	1548	Z0E90404T	2048	31.51	0.1256	1.00183
1	25-JAN-1991	1697	Z0E90604T	2048	31.65	0.1258	1.00144
1	15-FEB-1991	2425	Z0E90504T	2048	32.08	0.1261	1.00075
1	28-FEB-1991	2840	Z0E90704M	2048	31.76	0.1258	1.00135
1	12-MAR-1991	2952	Z0E90804T	2048	31.68	0.1256	1.00144
1	28-MAR-1991	3396	Z0E90904T	2048	31.81	0.1258	1.00126
1	9-JUN-1991	4099	Z0E90B04M	2048	32.02	0.1260	1.00100
2	12-NOV-1990	887	Z0E90C04T	2048	28.65	0.1240	1.00178
2	26-NOV-1990	1024	Z0E90D04T	2048	28.59	0.1241	1.00187
2	10-DEC-1990	1154	Z0E90E04T	2048	28.67	0.1242	1.00184
2	17-JAN-1991	1626	Z0E90F04T	2048	28.70	0.1241	1.00179
2	23-JAN-1991	1686	Z0E90H04T	2048	28.62	0.1241	1.00183
2	13-FEB-1991	2332	Z0E90G04T	2048	28.42	0.1240	1.00191
2	28-FEB-1991	2851	Z0E90I04M	2048	28.76	0.1243	1.00181
2	12-MAR-1991	2941	Z0E90J04T	2048	28.55	0.1243	1.00173
2	29-MAR-1991	3460	Z0E90K04T	2048	28.34	0.1241	1.00185
2	9-JUN-1991	4110	Z0E90M04T	2048	28.66	0.1244	1.00160

Figure 1
DETECTOR 1 FLAT FIELD LAMP
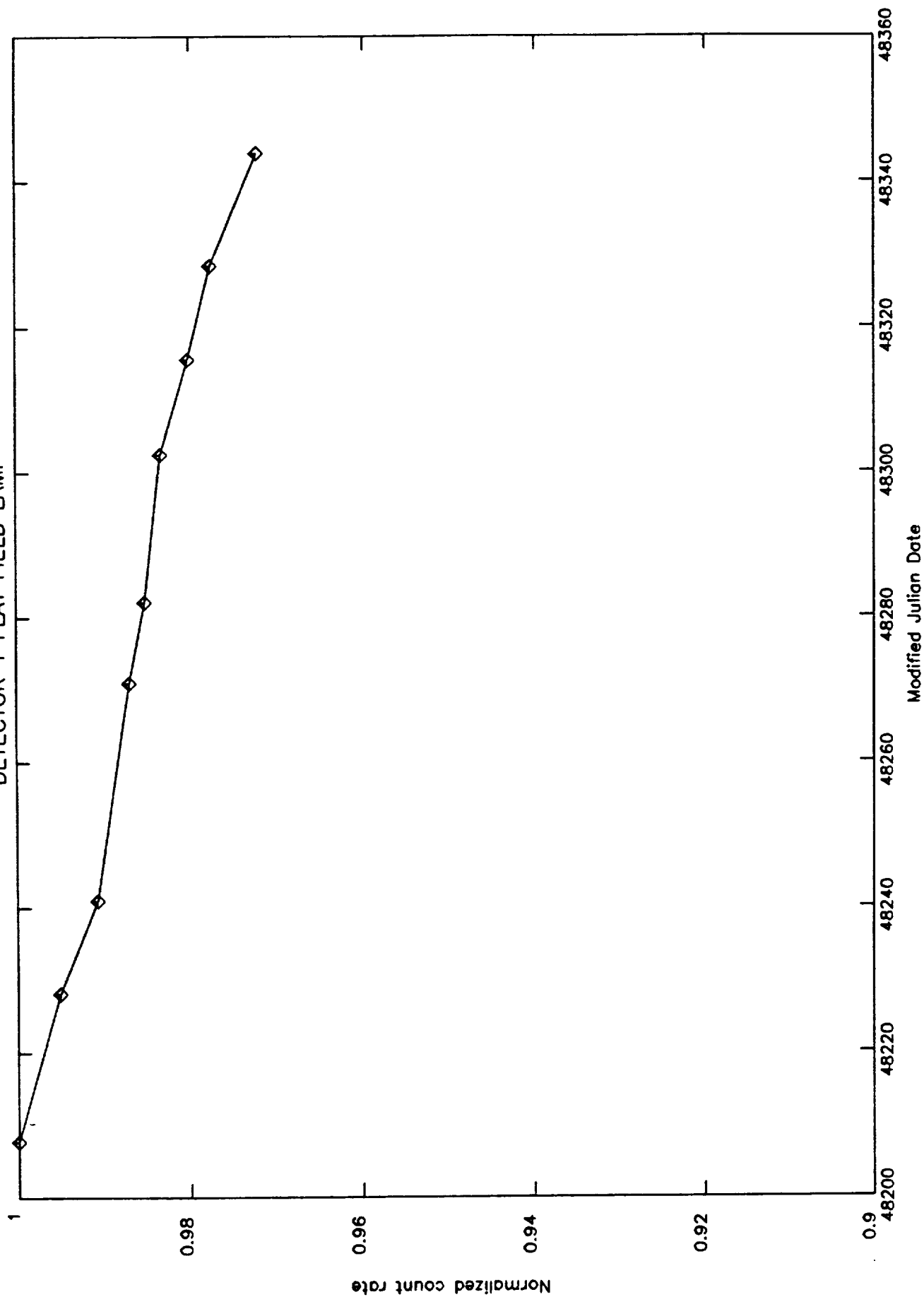
Figure 2
DETECTOR 2 FLAT FIELD LAMP

Normalized count rate

Modified Julian Date
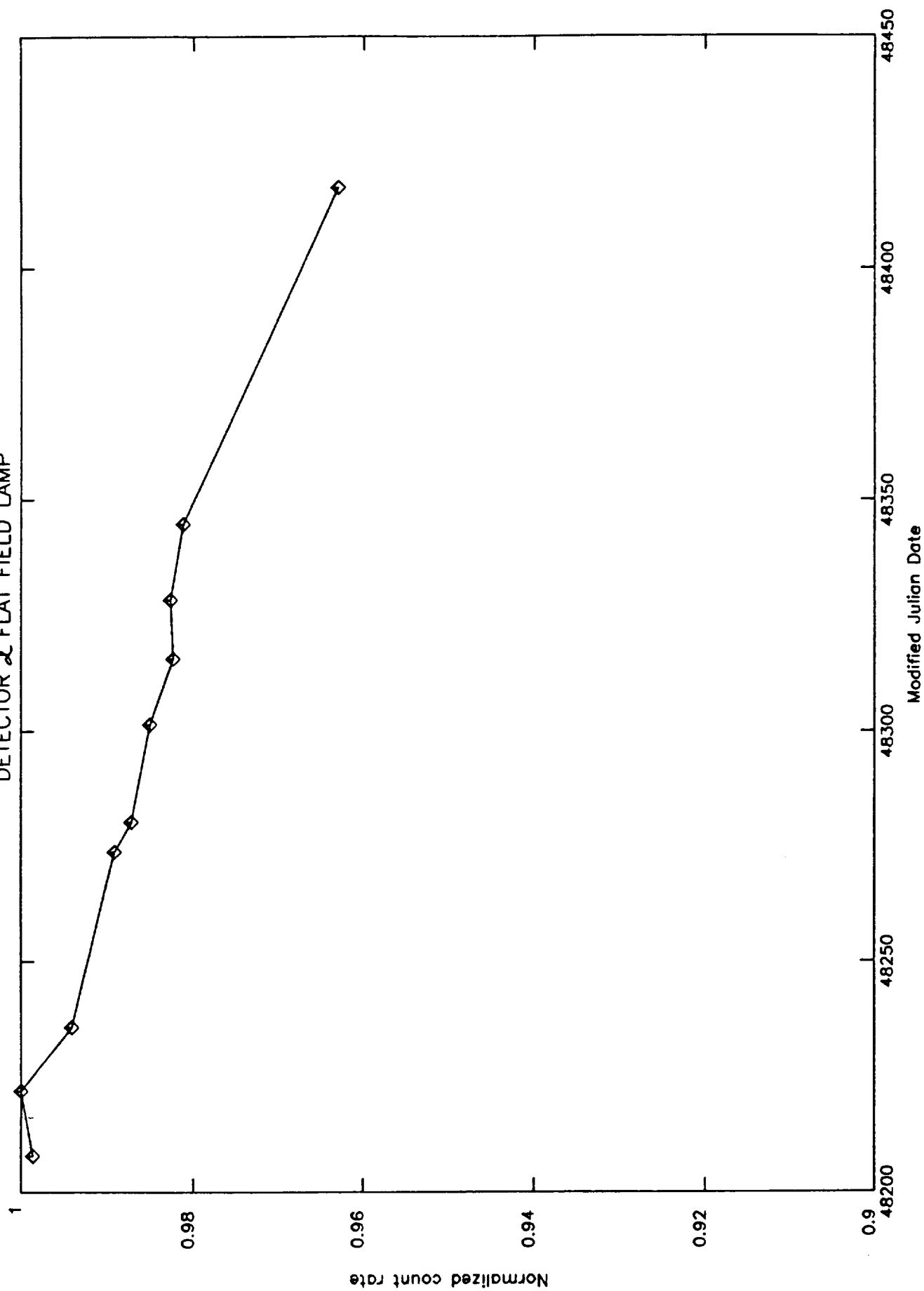
Figure 3

G-1   SC2
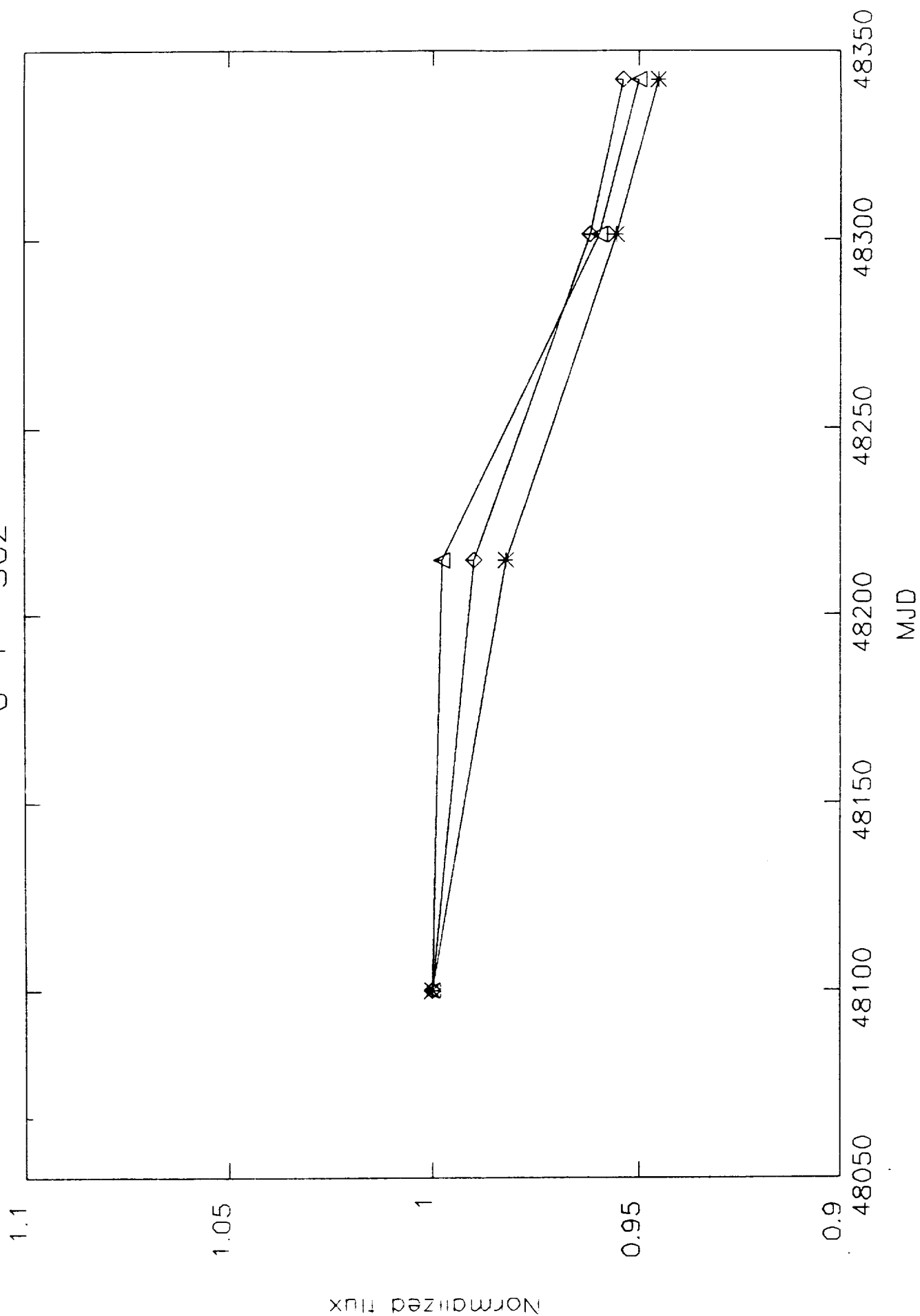
Figure 4   G-2   SC2
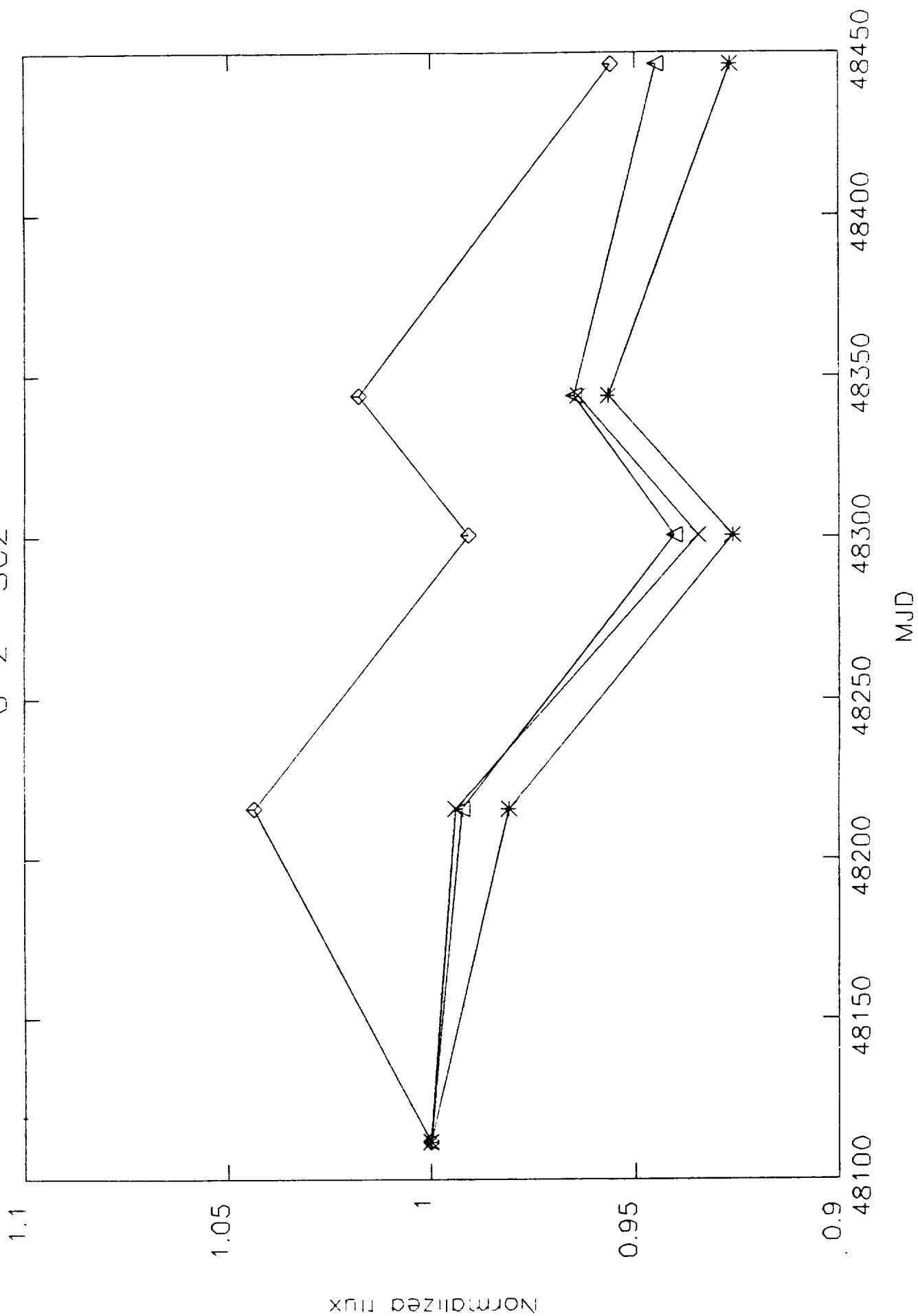
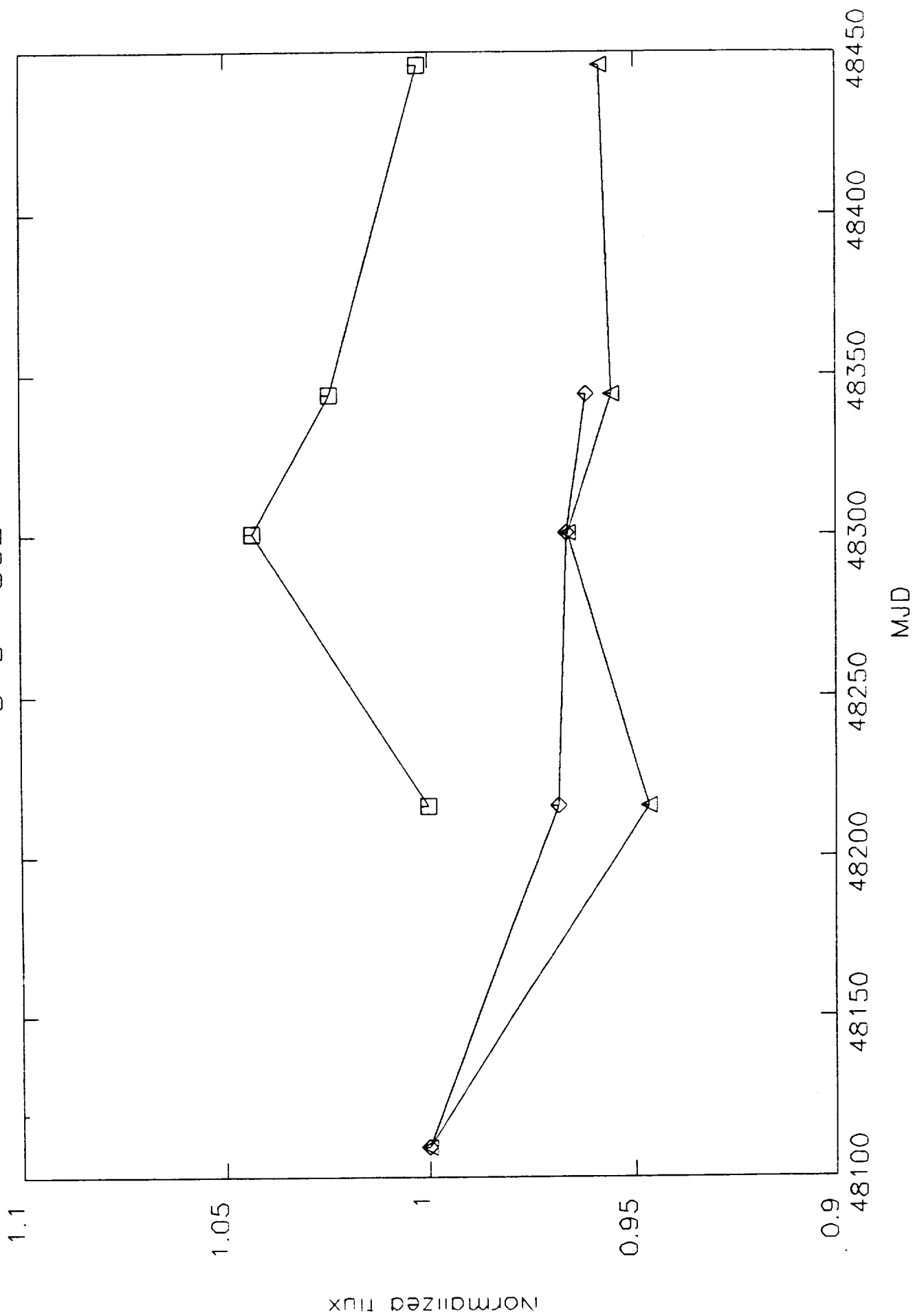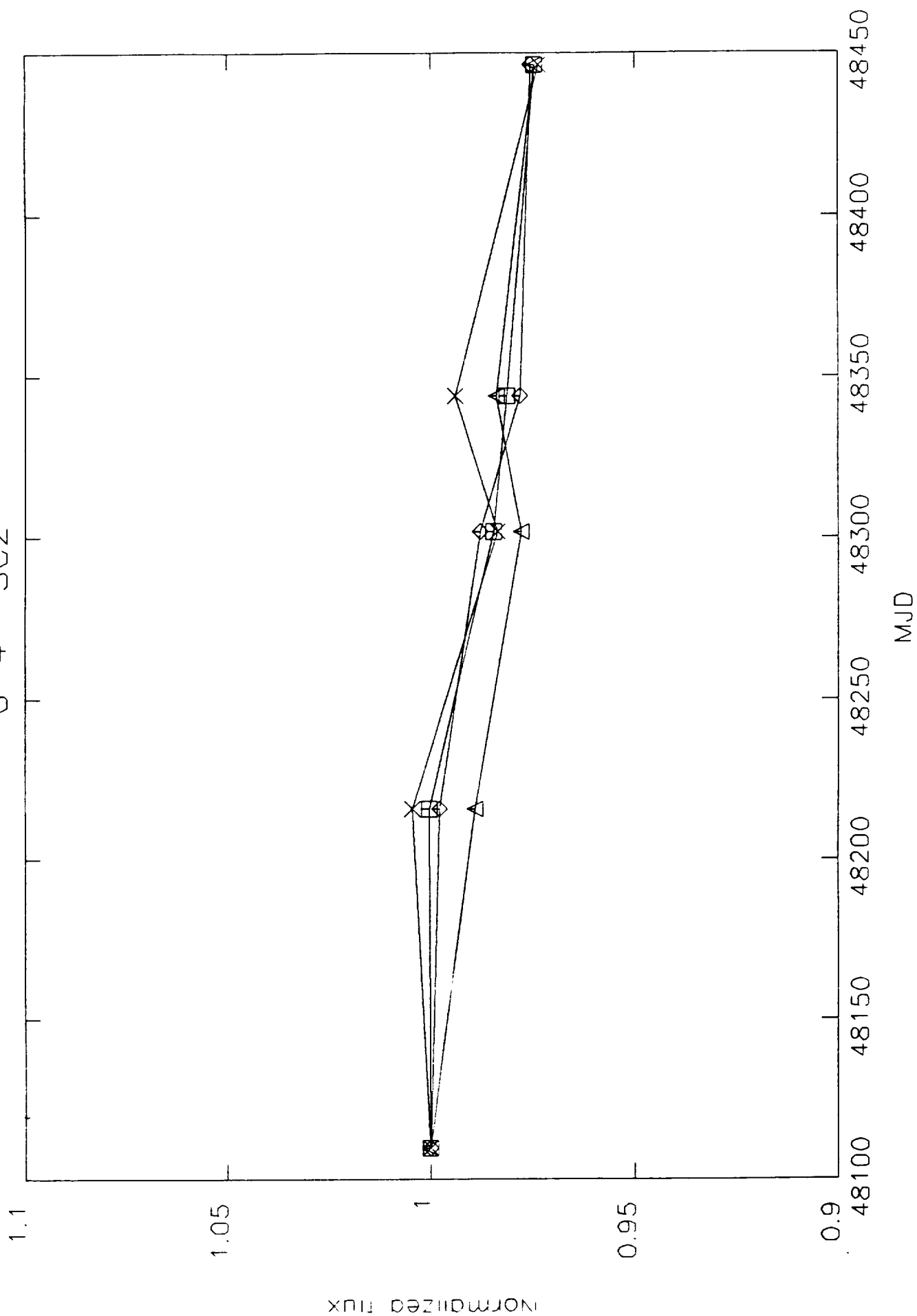Figure 5

G-3 SC2

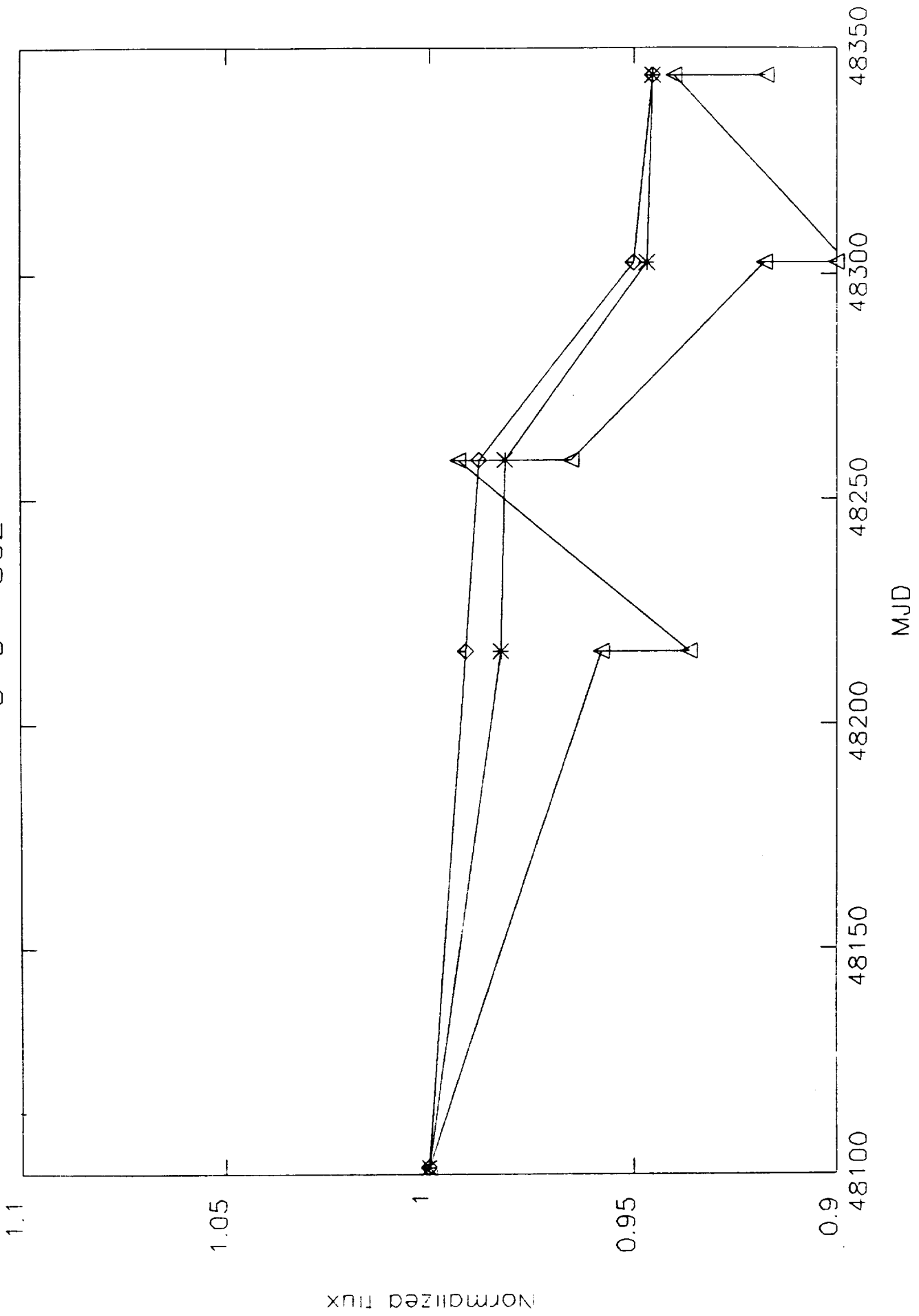Figure 6
G-4 SC2

Normalized flux

MJD

Figure 7

G-5 SC2

Normalized flux

MJD

GHRS Geomagnetic Image Motion

Don J. Lindler
July 31, 1991

ABSTRACT

We have measured the GHRS image motion do to the Earth's magnetic field and found that the motion at the diode array is approximately 50 microns (one diode)/Gauss for detector 2 and approximately 10 microns (0.2 diodes)/Gauss for detector 1. This motion can cause errors in target acquisition, errors in measured wavelengths, and can result in loss of spectral resolution. The impact of the magnetic motion can be minimized by limiting spectral observations to less than 5 minutes and by using the Double Locate mode of target acquisition.

1.0 INTRODUCTION

The GHRS OV/SV program has no formal tests for geomagnetic image motion. The best data for estimating the motion are the series of deflections calibrations (DEFCALs) taken during the coarse and fine alignment tests including;

Proposal	Date	Number of DEFCALs
2988	13-SEP-1990	12
2765	3-JAN-1991	15
2765	14-FEB-1991	15

Each test contained DEFCALs distributed over a 6 to 7 hour period. Each DEFCAL observation consists of an onboard measurement of the locations of the spectral calibration lamp apertures observed with mirror N1. The GHRS flight software computes the differences of the aperture locations from their nominal location to the nearest deflection unit (6.25 microns). These differences were used to track the X and Y image motion over the course of each test.

A second set of observations that were used to estimate the geomagnetic image motion were two observations designed to measure the carrousel stability over a period of one hour (proposal 2168, 15-Oct-1990). The data consisted of 150 spectral lamp observations taken over an hour in each Echelle mode. The carrousel position remained fixed during each sequence. We measured the motion in the x-direction (dispersion direction) of the digicons by cross correlation of each of the spectra with the first spectrum of the sequence.

To separate magnetic motion from other sources of image motion (e.g. thermal), we fit our results to the following model;

$$Motion = F(t) + S * B$$

where $F(t)$ (a quadratic function of time, t) is used to model non-geomagnetic motion, B is the earths magnetic field component in the appropriate direction, and S is a factor giving the geomagnetic motion in microns per Gauss. The coefficients of the quadratic function and S are solved simultaneously by a least squares fit.

2.0 Results

The results for the coarse and fine alignment DEFCAL sequences are shown in figures 1 through 6. The diamonds show the average difference of the two spectral calibration lamp apertures from their nominal positions. The dotted lines show the quadratic functions used to model non-geomagnetic motion. The solid lines show the models including both the geomagnetic and non-geomagnetic motion. The computed geomagnetic sensitivity factors were;

Date	Direction	Detector	S (microns/gauss)
13-SEP-1990	X	2	103
13-SEP-1990	Y	2	47
03-JAN-1991	X	2	49
03-JAN-1991	Y	2	44
14-FEB-1991	X	2	43
14-FEB-1991	Y	2	44

Expect for the first measurement, the observed magnetic motion for detector 2 is approximately one diode per Gauss. The quality of the present data makes it difficult to conclude that the magnetic sensitivity is variable. However, tests run on the Faint Object Spectrograph confirm that its geomagnetic sensitivity varies.

Figure 7 shows the spectral motion in the x-direction for data taken with Echelle B (detector 2) over a period of one hour. The sensitivity factor (39 microns/Gauss) for this observation is consistent with the DEFCAL observations. Figure 8, which shows the results for echelle A, indicates that detector 1 does not have a significant sensitivity to the Earth's magnetic field.

3.0 Recommendations

We make the following recommendations to combat the problems with geomagnetic image motion.

1) Limit detector 2 spectral observations to 5 minutes or less. There is no readout noise with digicons and the readout overhead time is minimal. Multiple readouts can be registered and coadded on the ground.

2) Use the double locate option in target acquisition. The success of your acquisition will depend on the minimization of the time between the deflection calibration and the target locate or peakup. This is particularly important if you intend to place the target in the small science aperture.

Figure 1

MN2 X-image motion   13-SEP-1990

Factor = 102.8 Microns/Gauss

RMS of fit = 3.7 Microns

Time (Minutes)

Motion (Microns)
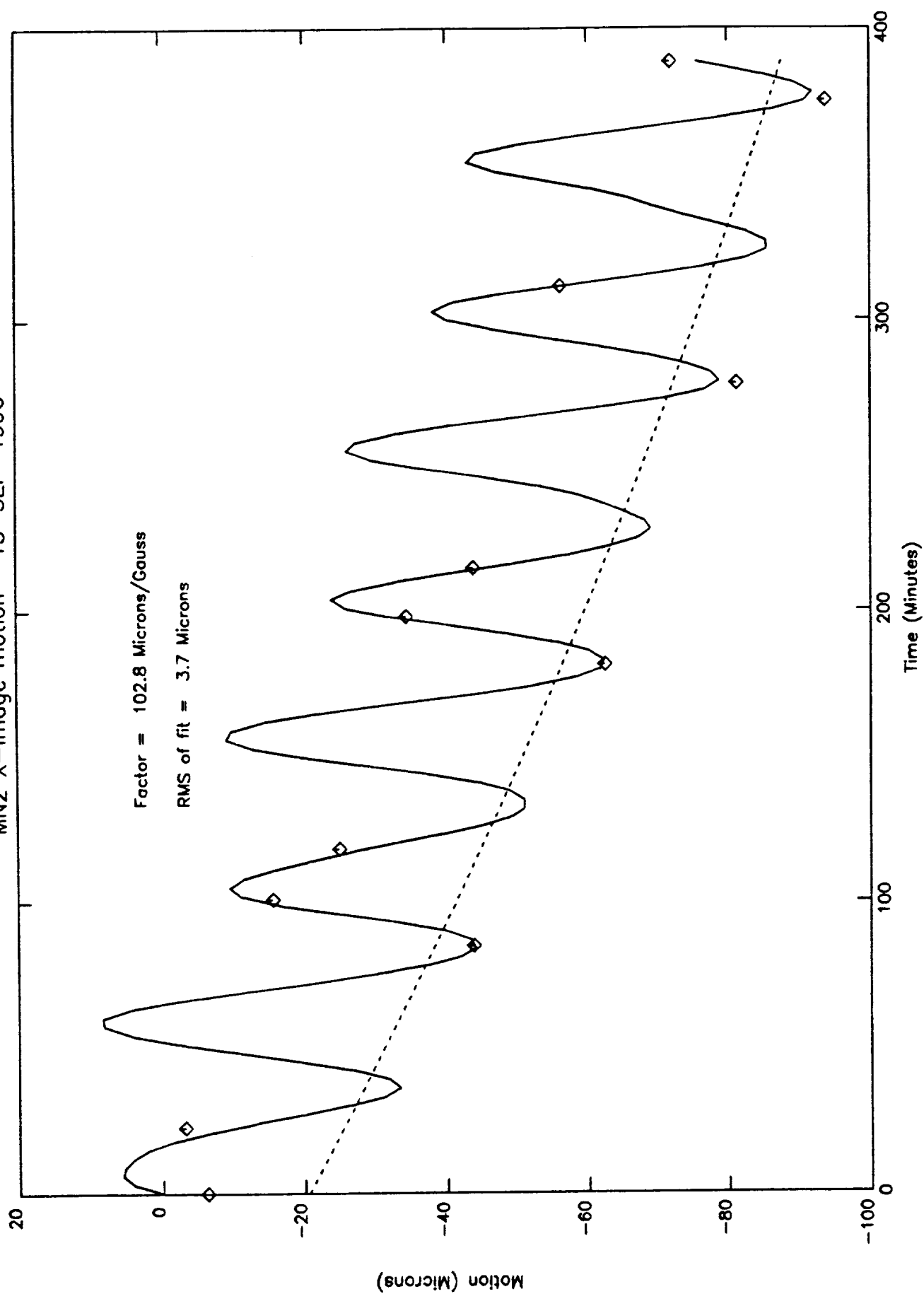
Figure 2

MN2 Y-image motion   13-SEP-1990

Factor =   46.7 Microns/Gauss

RMS of fit =   2.2 Microns

Time (Minutes)

Motion (Microns)
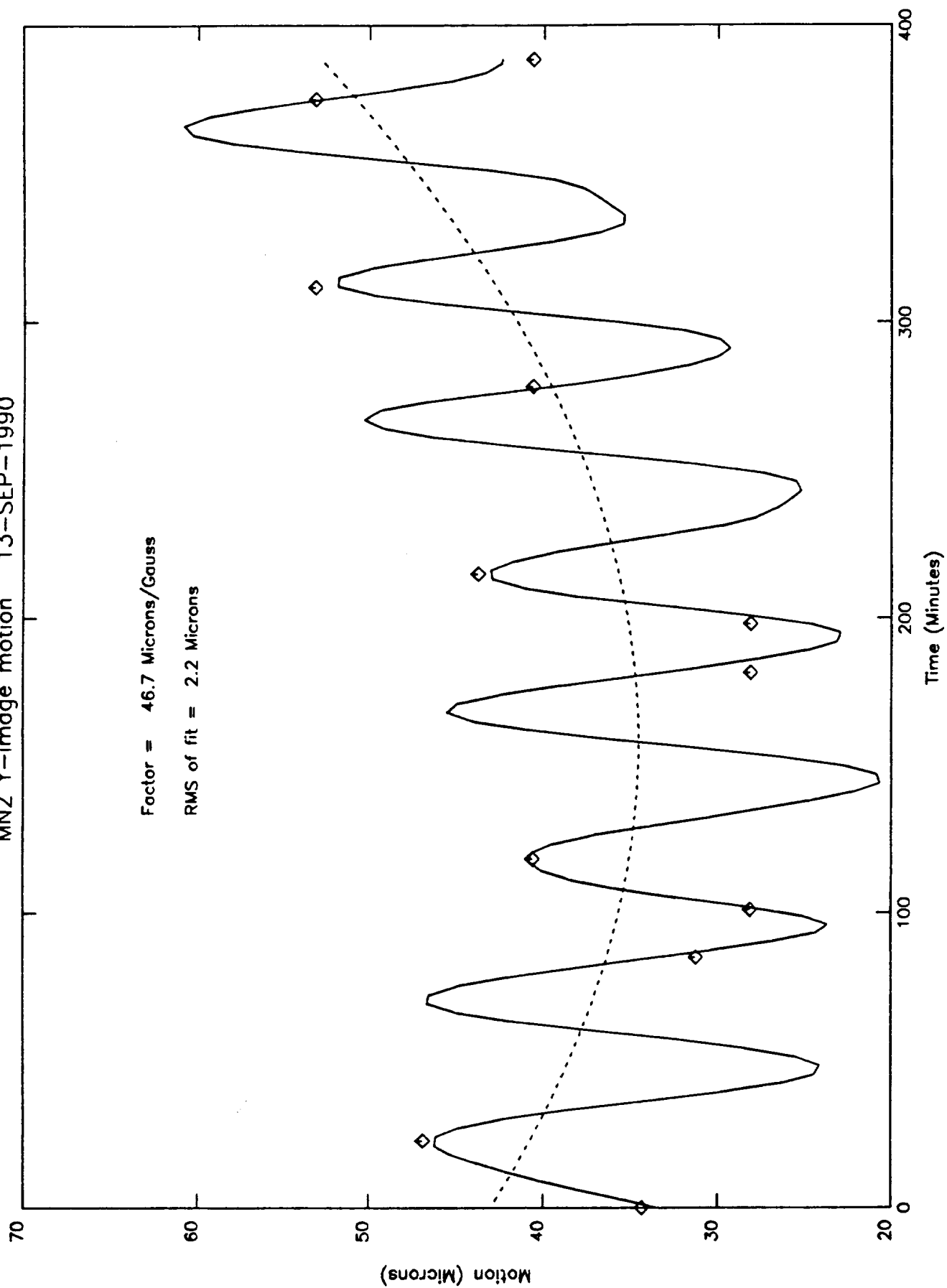
Figure 3

MN2 Y-image motion   14-FEB-1991

Factor =   43.2 Microns/Gauss

RMS of fit =   3.5 Microns

Motion (Microns)

Time (Minutes)
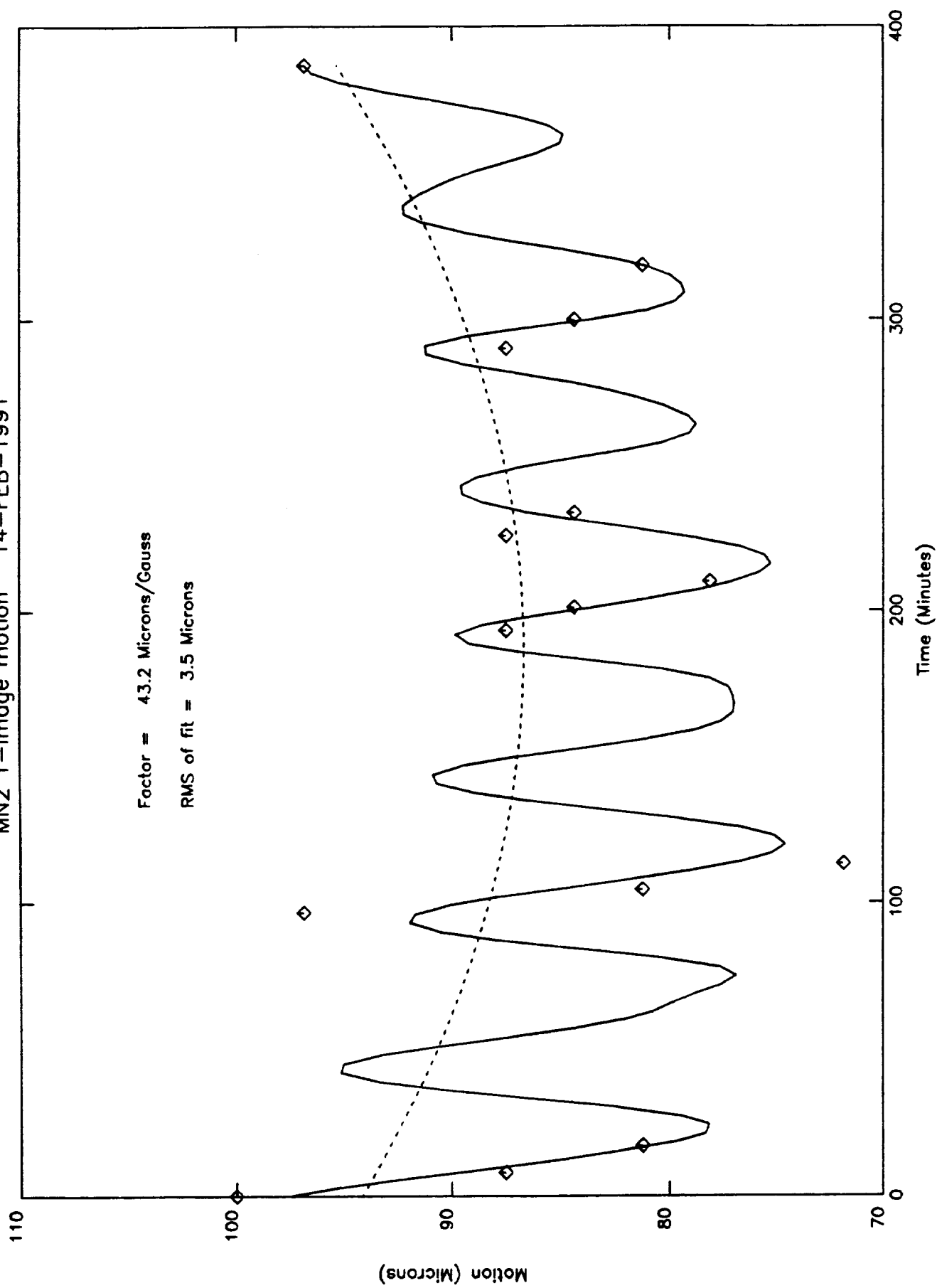
Figure 4

MN2 X-image motion 14-FEB-1991

Factor = 44.1 Microns/Gauss

RMS of fit = 1.2 Microns

Time (Minutes)

Motion (Microns)
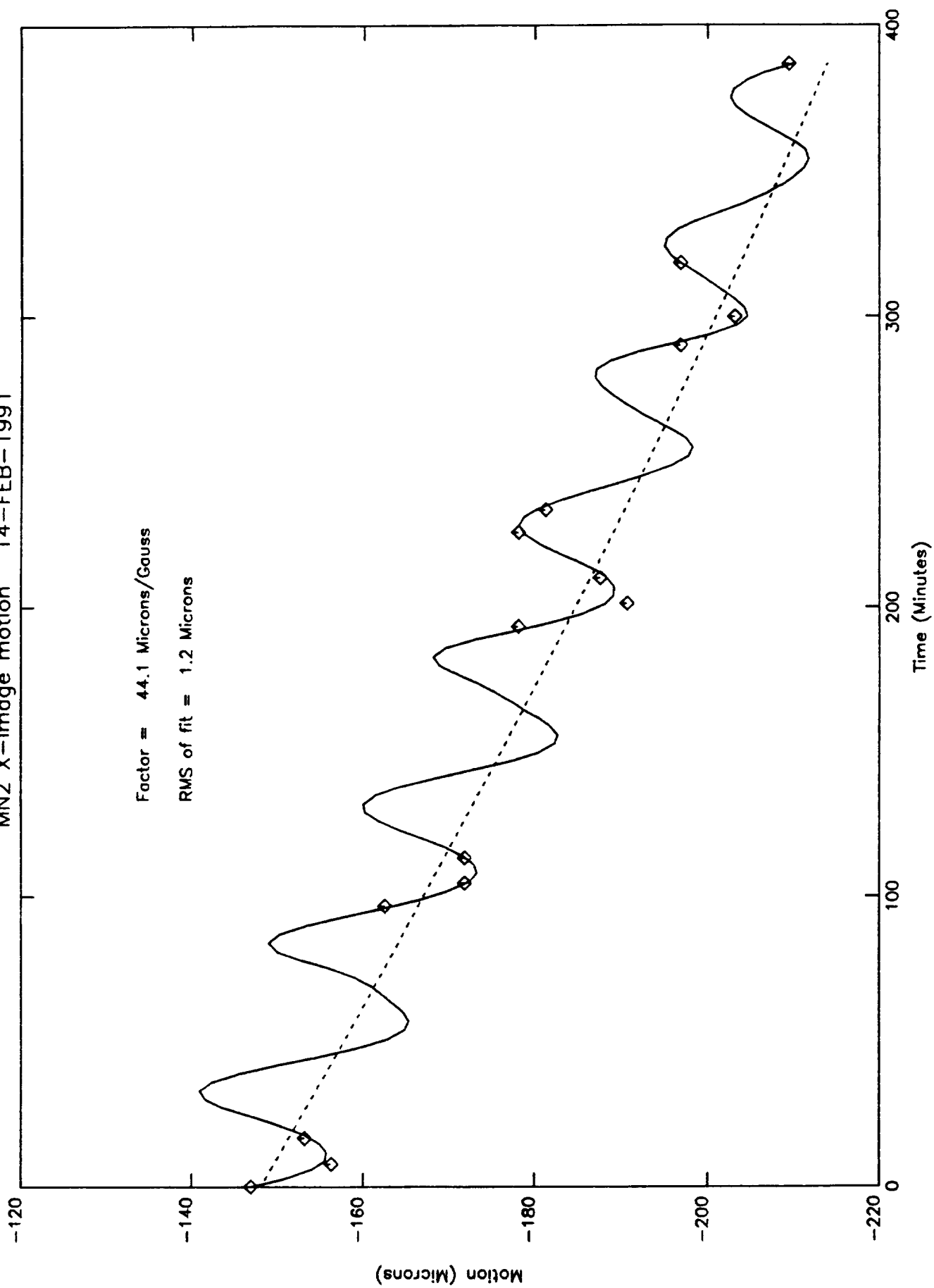
Figure 5

MN2 X-image motion   3-JAN-1991

Factor =   49.4 Microns/Gauss

RMS of fit = 1.4 Microns

Time (Minutes)

Motion (Microns)
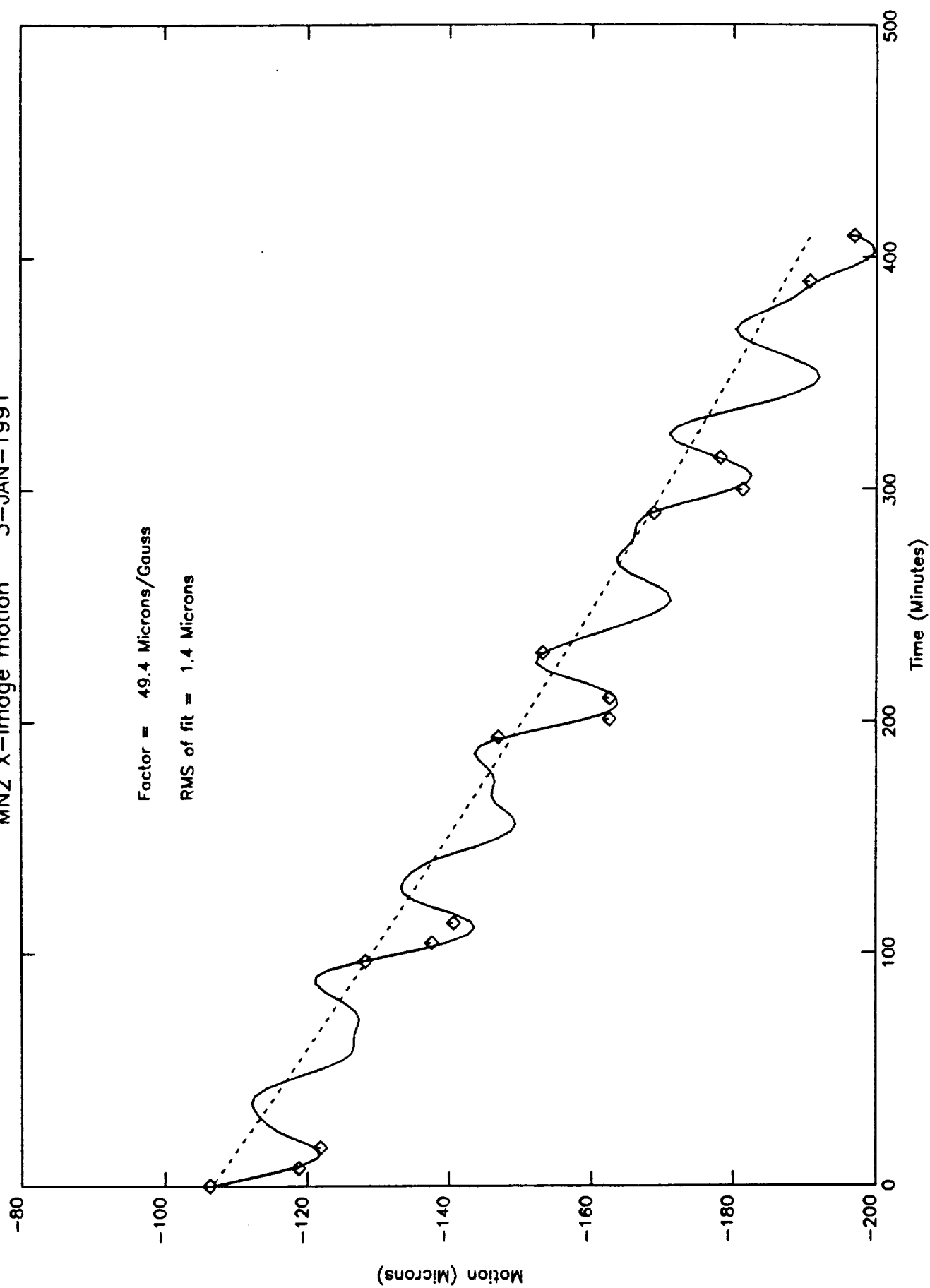
Figure 6

MN2 Y-image motion   3-JAN-1991

Factor =   44.0 Microns/Gauss

RMS of fit = 2.7 Microns

Time (Minutes)

Motion (Microns)
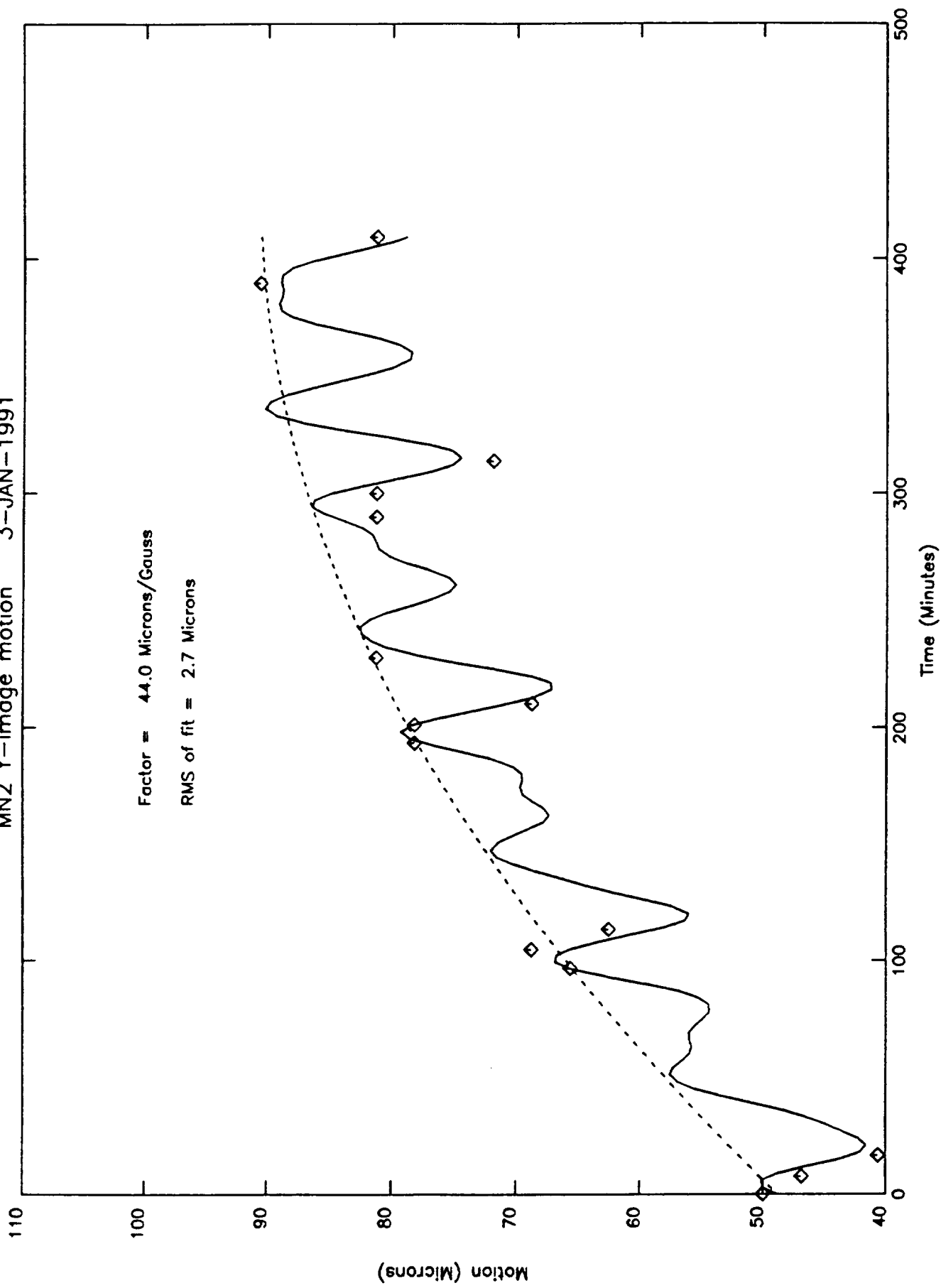
Figure 7

E-B X-image motion   15-OCT-1990

Factor = -38.9 Microns/Gauss

RMS of fit = 1.6 Microns

Motion (Microns)

Time (Minutes)
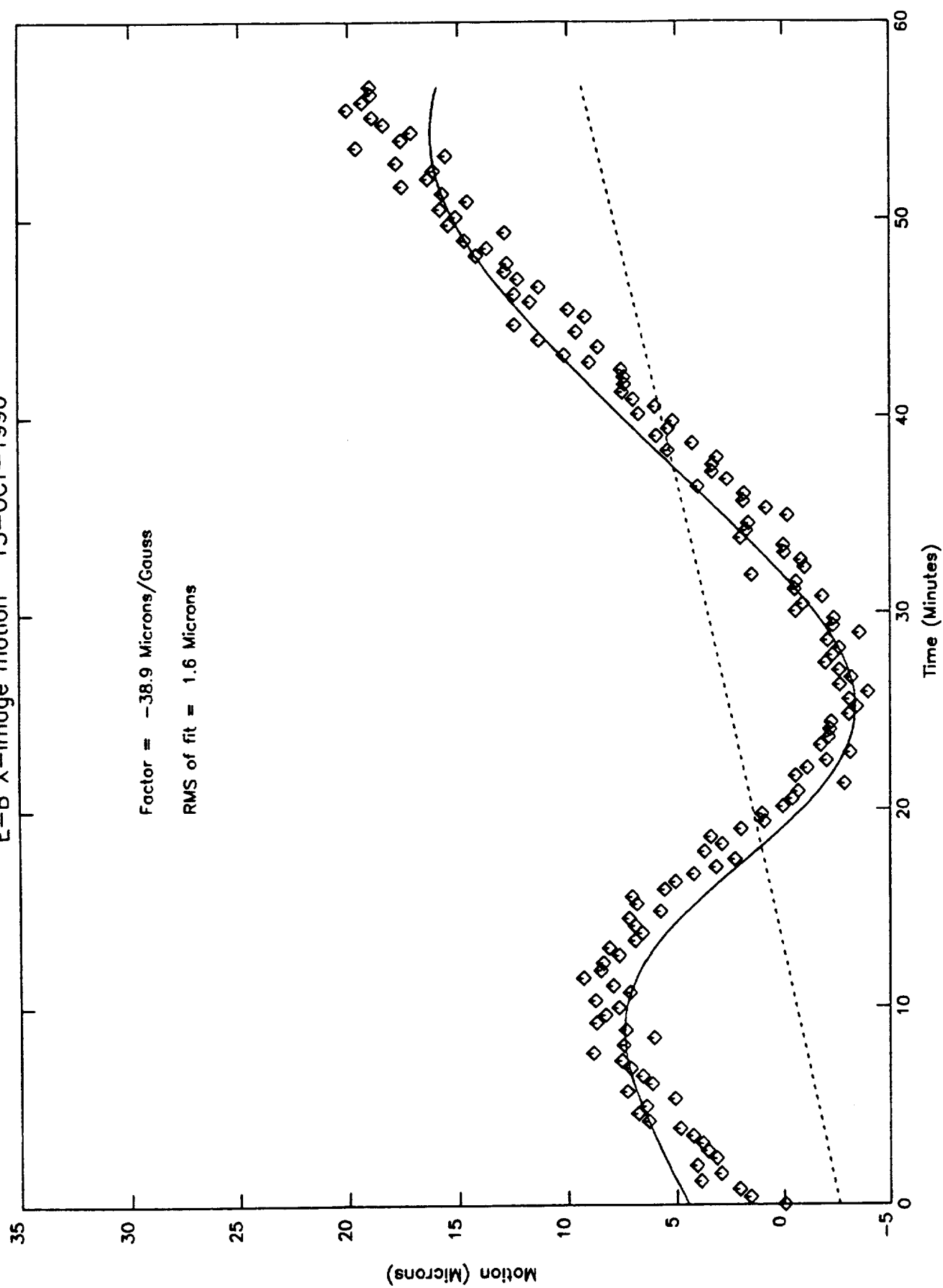
Figure 8

E-A X-image motion 15-OCT-1990

Factor = 10.2 Microns/Gauss

RMS of fit = 1.0 Microns

Motion (Microns)

Time (Minutes)
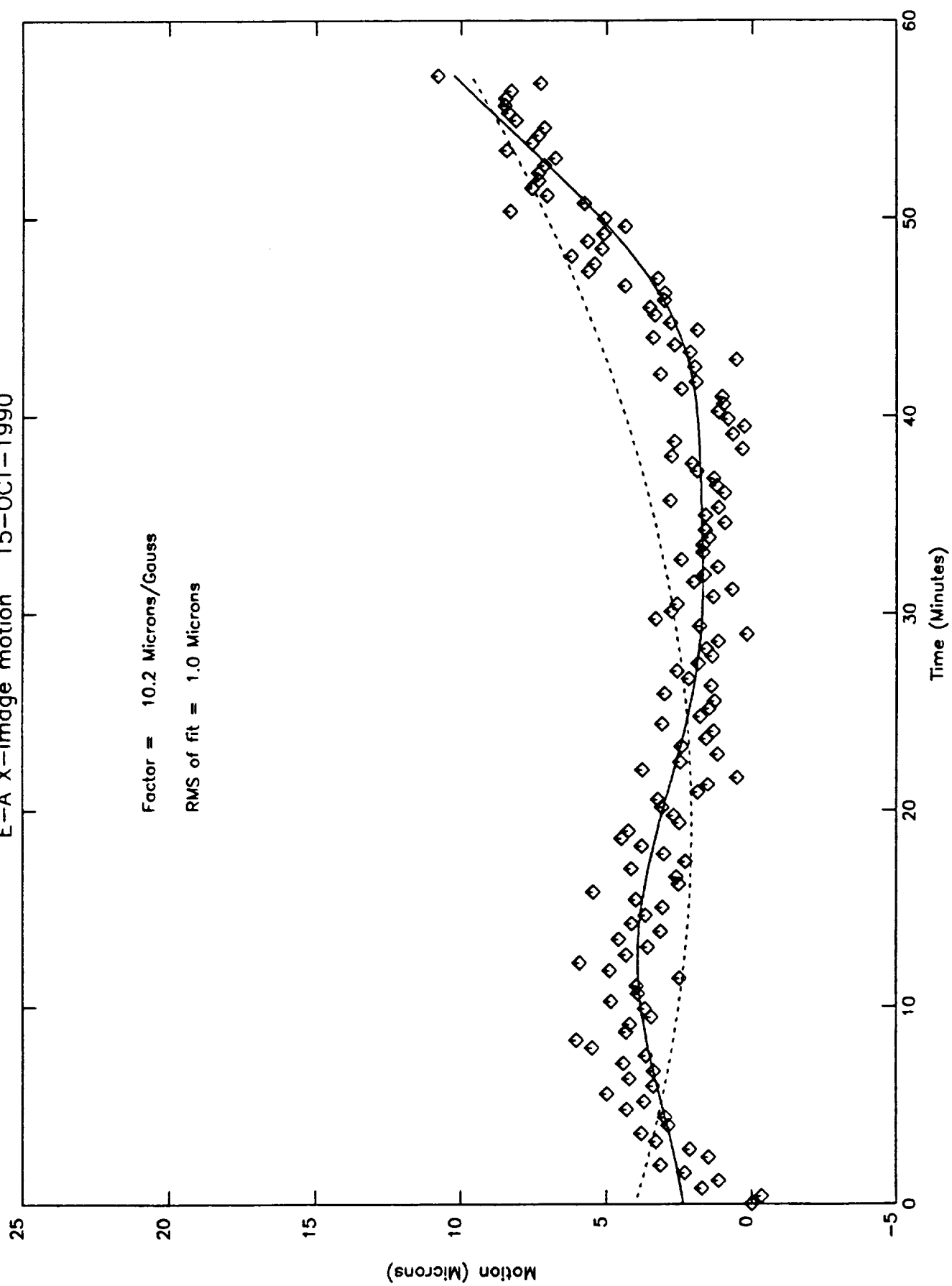
GHRS OV/SV Wavelength Calibration

Don J. Lindler
14 August 1991

ABSTRACT

We have analyzed the GHRS OV/SV spectral calibration lamp observations and found that an average dispersion coefficient table with linear thermal motion models can be used to compute wavelengths for science observations to better than one photocathode sample unit (50 microns). If spectral calibration lamp observations are taken along with the science observations, the errors can be decreased to .17 sample units (one sigma error), which equals 0.5 km/s in the echelle modes.

1.0 Introduction

We used the following process to construct the dispersion coefficient table required by the standard GHRS reduction routine, CALHRS.

> 1) Compute the dispersion relation for multiple carrousel positions and thermal conditions using routine WAVECAL (section 2.0).

> 2) Derive each dispersion coefficient as a polynomial function of carrousel position (section 3.0).

> 5) Construct a thermally induced motion model by fitting the residuals of the fit in step 2 as a linear function of a selected GHRS thermistor reading (section 4.0).

> 8) Generate a dispersion coefficient table on a finely spaced carrousel position grid (section 5.0).

The above procedure was repeated for each grating mode.

2.0 The GHRS dispersion relation.

The dispersion equation used by the GHRS standard reduction routine CALHRS is given by:

$$s = a0 + a1*m*w + a2*m*m*w + a2*m + a4*w +$$
$$a5*m*m*w + a6*m*w*w + a7*m*m*m*w*w*w$$

    s - is the photocathode sample position
    w - is the wavelength
    m - is the spectral order (1 for first order gratings)
    a0, a1, ... a7 - are dispersion coefficients which vary
          with carrousel position

We computed the dispersion coefficients using observations of the internal spectral calibration lamps SC1 and SC2 with GHRS/IDL routine WAVECAL. WAVECAL finds the positions of spectral lines in the a platinum/neon hollow cathode lamp line list (Reader, 1990). WAVECAL then computes the dispersion coefficients by a least squares fit which minimizes the sum of the squares of the difference between the observed spectral line positions and those computed by the dispersion relation.

We have found that the following non-zero coefficients are required for each of the gratings:

        G-1 (G140M)   a0, a1, a2
        G-2 (G160M)   a0, a1, a2, a7
        G-3 (G200M)   a0, a1, a2, a7
        G-4 (G270M)   a0, a1, a2, a7
        G-5 (G140L)   a0, a1, a2
        E-A (ECH-A)   a0, a1, a2, a4
        E-B (ECH-B)   a0, a1, a2, a4, a7

The cubic coefficient, a7, is required only for the detector 2 gratings and coefficient a4 is redundant with the a1 coefficient for the first order gratings where the spectral order, m, equals 1. Analysis of the residuals of the dispersion coefficient fits indicate that coefficients a3 and a5 are not required.

Experiments have shown that the cubic coefficient, a7, can not be accurately fit for every carrousel position. The spectral calibration lamp spectra have an inadequate number of spectral lines or poorly spatially distributed spectral lines at many of the carrousel positions. The cubic term does not, however, vary significantly with carrousel position. This allows us to compute a constant a7 for each grating by fitting all carrousel positions simultaneously. For example, Figure 1, shows the residuals (observed minus fitted spectral line positions) for all G-2 observations taken at multiple carrousel positions when no cubic term is used. A cubic polynomial was then fit to these residuals to give an a7 coefficient applicable to all carrousel positions for the grating. We then reran WAVECAL on each observation with a fit to the non-cubic coefficients while holding the cubic term, a7, fixed at the the value computed from all carrousel

positions. Figure 2 shows the same plot as figure 1 when cubic term is included.

3.0 Dispersion coefficient variations with carrousel position.

The dispersion coefficients computed by WAVECAL do not vary smoothly with carrousel position (Cushman, Ebbets, and Holmes, 1986). This is particularly true of the a0 and a1 terms. These unpredictable variations between carrousel positions make it difficult to analyze thermal variations and to compute dispersion coefficients for carrousel positions without a corresponding spectral calibration lamp observation. The solution to this problem is to transform the coefficients to a different coordinate system in which they vary smoothly. The following coordinate system satisfies this requirement.

$$s = f0 + f1*x + f2*x*x + f3*x*x*x + f4*y$$

$$x = m*w - mc \cdot wc$$
$$y = w - wc$$

mc is the central order (42 for E-A, 25 for E-B, and
        1 for the first order gratings)
wc is the central wavelength at the given carrousel position
        computed by the carrousel equation:

$$wc = \frac{A}{mc} * SIN\left(\frac{C - R}{10430.378}\right)$$

R is the carrousel position
A and C are coefficients which vary with grating mode and
        are determined by a non-linear least squares fit
        to the observed wavelengths at photocathode sample
        position 280.0.

The coefficients f0, ...,f1 are calculated from the dispersion coefficients a0, ..., a1 at carrousel position R by:

$$k = mc*wc$$
$$f0 = a0 + a1*k + a2*k*k + a7*k*k*k + a4*wc$$
$$f1 = a1 + 2*a2*k + 3*a7*k*k$$
$$f2 = a2 + 3*a7*k$$
$$f3 = a7$$
$$f4 = a4$$

We can now fully characterize the dispersion relation for all carrousel positions of a grating by fitting polynomials of carrousel position to the f0, f1, f2, f3, and f4 terms:

$$f0 = F00 + F01*R + F02*R*R$$

Table 1

Coefficients for an Average Dispersion Model for Each Grating Mode

GRATING	G-1	G-2	G-3	G-4	G-5	E-A	E-B
A	3301.5964	4020.5509	4615.4945	5539.2806	33003.863	62885.234	63193.068
C	11107.568	54807.929	30600.949	14887.264	49184.376	39021.834	50575.350
MC	1	1	1	1	1	42	25
F00	256.62134	-728.15796	280.88486	227.01079	279.89880	409.69528	472.65100
F01	7.25379633E-03	3.98388132E-02	-6.91596724E-05	1.12166228E-02	2.07594940E-06	-9.43191350E-03	-9.84503608E-03
F02	-5.58414172E-07	-3.93529803E-07	1.35064215E-09	-5.91657567E-07	0	1.71468784E-07	1.25765894E-07
F10	26.326927	233.64894	76.723503	21.845684	1.0548606	37.647785	96.412254
F11	-1.90600345E-03	-8.18108767E-03	-4.44889721E-03	-1.79814536E-03	1.42177905E-05	-2.36142310E-03	-4.55840025E-03
F12	1.03189940E-07	7.60026211E-08	7.62773738E-08	6.76958010E-08	0	3.83489827E-08	5.46387788E-08
F20	1.07031828E-02	1.03096245E-02	1.43394654E-03	3.32586048E-03	-1.94696506E-04	1.33190514E-03	2.69511109E-03
F21	-9.30480837E-07	-1.62813990E-07	6.44372777E-09	-2.06343472E-07	4.43220616E-09	-4.47929516E-08	-6.60436541E-08
F22	0	0	0	0	0	0	0
F30	0	-8.78327893E-05	-6.07879721E-05	-3.89920402E-05	0	0	-1.17056088E-07
F31	0	0	0	0	0	0	0
F32	0	0	0	0	0	0	0
F40	0	0	0	0	0	-2.02021468E-02	-4.62628808E-03
F41	0	0	0	0	0	8.05789341E-07	1.21845346E-07
F42	0	0	0	0	0	0	0

$$f1 = F10 + F11*R + F12*R*R$$
$$\ldots$$
$$f4 = F40 + F41*R + F42*R*R$$

where R is the carrousel position and Fij are the coefficients of the polynomials. The derived values of Fij for all grating modes are given in table 1.

4.0 Spectral Motion

The residuals of the polynomial fits to the f0, f1. ... and f4 terms in section 3.0 can be used to analyze changes in the dispersion relation with respect to temperature, time and the earths magnetic field. Since we had a large number of wavelength calibration observations for each grating mode, we treated the values of the coefficients, Fij, representative for average conditions. The difference of the dispersion coefficients for each individual spectral calibration lamp observation from the values of the polynomial fits (which we will call the predicted values) can be attributed to thermal motion, geomagnetically induced motion, carrousel repeatability, instrument aging, ect. The largest differences were found in the f0, or constant, term. Changes in this term represent movement of the entire spectral format. We have correlated the offsets of the f0 coefficient with temperature, time, and the relevant component of the Earth's magnetic field vector. The largest source of variation in the f0 term is caused by thermal effects. Table 2 gives the results of linear fits to the offsets for 22 different temperatures listed in table 3. The RMS of the offsets of f0 from the predicted values and the maximum of the absolute value of the offsets are given in the row titled "No Fit". The other rows give the RMS and maximum of absolute value of the residuals of a linear fit of the offsets to the specified thermistor values. The RMS is an estimate of the correlation with the specified thermistor reading. If the RMS is near that of the "No Fit" value, no significant correlation exists. The results of the best correlations are shown in Figures 3 through 9. The offsets of f0 from the predicted values for each spectral calibration observation are shown as plus marks (+). The solid lines show the linear thermal models.

The values of the RMS columns in table 2 are useful for determining the accuracy of the wavelengths assigned by CALHRS. If an average dispersion coefficient table is used without application of a thermal model, the "No Fit" rows in table 2 give an indication of the typical errors. For example, the typical error for grating 4 would be 2 sample units (100 microns) and in some cases could be almost 4 sample units (200 microns). Using the linear thermal model option of CALHRS reduces the typical grating 4 error to 0.25 sample units.

Table 2

Linear Thermal Model for Spectral Motion in the Dispersion direction

RMS - RMS of the a linear fit to the specified temperature location (sample units)
MAX - Distance of data point with maximum deviation from the fit (sample units)
SLOPE - slope of the fit (sample units/degree)

	G-1			G-2			G-3			G-4		
	RMS	MAX	SLOPE	RMS	MAX	SLOPE	RMS	MAX	SLOPE	RMS	MAX	SLOPE
No Fit	0.39	0.98		0.54	1.28		1.61	3.31		1.95	3.74	
ZRIUTA	0.20	0.47	-0.66E-01	0.27	0.72	-0.11E+00	0.47	1.17	-0.22E+00	0.57	1.24	-0.33E+00
ZRIUTB	0.19	0.47	-0.65E-01	0.25	0.64	-0.10E+00	0.50	1.16	-0.20E+00	0.67	1.38	-0.28E+00
ZDETT1	0.26	0.58	-0.14E+00	0.49	1.33	-0.11E+00	0.89	2.20	-0.57E+00	0.99	2.18	-0.73E+00
ZDETT2	0.27	0.68	-0.11E+00	0.33	0.83	-0.24E+00	0.47	1.29	-0.46E+00	0.29	0.98	-0.61E+00
ZDEBTF	0.19	0.40	-0.33E-01	0.25	0.71	-0.52E-01	0.47	1.19	-0.10E+00	0.68	1.44	-0.14E+00
ZPABT1	0.25	0.77	-0.69E-01	0.52	1.34	-0.44E-01	1.06	2.59	-0.38E+00	1.36	2.71	-0.43E+00
ZPABT2	0.28	0.73	-0.77E-01	0.29	1.04	-0.96E-01	0.57	1.60	-0.20E+00	0.89	2.20	-0.23E+00
ZMEBT1	0.19	0.44	-0.59E-01	0.25	0.68	-0.97E-01	0.53	1.27	-0.20E+00	0.77	1.63	-0.29E+00
ZMEBT2	0.19	0.45	-0.62E-01	0.27	0.68	-0.92E-01	0.55	1.33	-0.19E+00	0.76	1.52	-0.28E+00
ZFIAT	0.25	0.60	-0.12E+00	0.39	0.97	-0.22E+00	0.42	0.89	-0.53E+00	0.47	1.55	-0.66E+00
ZFIBT	0.26	0.67	-0.18E+00	0.46	1.13	-0.27E+00	0.61	1.44	-0.90E+00	0.94	2.74	-0.11E+01
ZFICT	0.22	0.59	-0.99E-01	0.34	0.90	-0.17E+00	0.37	0.93	-0.37E+00	0.43	1.57	-0.50E+00
ZCST	0.27	0.65	-0.15E+00	0.36	0.95	-0.26E+00	0.49	1.16	-0.62E+00	0.24	0.73	-0.76E+00
ZSCT1	0.28	0.68	-0.12E+00	0.54	1.28	-0.91E-04	1.61	3.31	-0.10E-02	1.95	3.74	-0.28E-03
ZSCT2	0.39	0.98	0.13E-03	0.54	1.30	-0.80E-03	1.60	3.09	-0.19E-01	1.92	4.11	-0.24E-01
ZHVPST1	0.24	0.56	-0.15E+00	0.54	1.28	-0.91E-04	1.61	3.31	-0.10E-02	1.95	3.74	-0.28E-03
ZHVPST2	0.39	0.98	0.13E-03	0.54	1.33	0.21E-02	1.60	3.09	-0.15E-01	1.94	3.91	-0.10E-01
ZDT11	0.24	0.58	-0.15E+00	0.54	1.28	-0.71E-03	1.60	3.40	0.12E-01	1.93	3.85	0.17E-01
ZDT12	0.39	0.98	0.13E-03	0.54	1.29	-0.13E-02	1.58	3.39	-0.24E-01	1.89	3.85	-0.32E-01
ZDRT	0.24	0.72	-0.14E+00	0.38	0.96	-0.25E+00	0.51	1.36	-0.60E+00	0.68	2.21	-0.81E+01
ZOBBT	0.27	0.69	-0.18E+00	0.40	1.07	-0.31E+00	0.53	1.34	-0.82E+00	0.42	0.88	-0.10E+01
ZDEBTR	0.19	0.39	-0.34E-01	0.26	0.74	-0.52E-01	0.48	1.19	-0.10E+00	0.68	1.44	-0.14E+00

	G-5			E-A			E-B		
	RMS	MAX	SLOPE	RMS	MAX	SLOPE	RMS	MAX	SLOPE
No Fit	0.90	2.01		0.90	1.93		0.54	1.02	
ZRIUTA	0.87	2.15	0.44E-01	0.43	0.79	-0.16E+00	0.31	0.56	-0.92E-01
ZRIUTB	0.87	2.13	0.40E-01	0.40	0.74	-0.16E+00	0.30	0.57	-0.88E-01
ZDETT1	0.77	1.82	0.17E+00	0.26	0.49	-0.39E+00	0.42	0.89	-0.18E+00
ZDETT2	0.79	1.88	0.16E+00	0.21	0.43	-0.25E+00	0.33	0.70	-0.21E+00
ZDEBTF	0.88	2.16	0.18E-01	0.56	1.22	-0.72E-01	0.28	0.55	-0.44E-01
ZPABT1	0.86	2.15	0.42E-01	0.84	2.11	-0.77E-01	0.46	0.88	-0.68E-01
ZPABT2	0.88	2.04	0.46E-01	0.32	0.73	-0.17E+00	0.36	0.77	-0.89E-01
ZMEBT1	0.88	2.12	0.26E-01	0.58	1.40	-0.13E+00	0.30	0.60	-0.78E-01
ZMEBT2	0.88	2.13	0.35E-01	0.45	0.96	-0.15E+00	0.29	0.54	-0.81E-01
ZFIAT	0.77	1.87	0.26E+00	0.19	0.48	-0.28E+00	0.42	0.88	-0.15E+00
ZFIBT	0.77	1.71	0.11E+00	0.20	0.45	-0.43E+00	0.43	0.89	-0.23E+00
ZFICT	0.80	1.97	0.20E+00	0.19	0.41	-0.23E+00	0.34	0.72	-0.15E+00
ZCST	0.78	1.92	0.18E+00	0.17	0.37	-0.37E+00	0.31	0.69	-0.29E+00
ZSCT1	0.77	2.06	-0.15E-03	0.57	1.44	-0.21E+00	0.54	1.02	0.73E-03
ZSCT2	0.90	2.01	0.19E+00	0.90	1.93	0.10E-02	0.53	0.97	0.78E-02
ZHVPST1	0.75	1.81	-0.15E-03	0.27	0.55	-0.43E+00	0.54	1.02	0.73E-03
ZHVPST2	0.90	2.01	0.18E+00	0.90	1.93	0.10E-02	0.52	0.95	0.98E-02
ZDT11	0.77	1.95	-0.15E-03	0.30	0.65	-0.44E+00	0.45	0.81	-0.20E+00
ZDT12	0.90	2.01	0.18E+00	0.90	1.93	0.10E-02	0.54	1.02	0.22E-03
ZDRT	0.78	1.83	0.18E+00	0.19	0.41	-0.33E+00	0.37	0.78	-0.22E+00
ZOBBT	0.76	1.81	0.27E+00	0.21	0.50	-0.45E+00	0.37	0.87	-0.32E+00
ZDEBTR	0.88	2.15	0.17E-01	0.53	1.20	-0.74E-01	0.29	0.54	-0.44E-01

Table 3

Table 2 Thermistor Locations

ZRIUTA	RIU A temperature
ZRIUTB	RIU B temperature
ZDETT1	Detector 1 temperature
ZDETT2	Detector 2 temperature
ZDEBTF	DEB front post-amp temperature
ZDEBTR	DEB rear post-amp temperature
ZPABT1	Detector 1 preamp assembly box temperature
ZPABT2	Detector 2 preamp assembly box temperature
ZMEBT1	Main electronic box 1 temperature
ZMEBT2	Main electronic box 2 temperature
ZFIAT	Fixture interface A temperature
ZFIBT	Fixture interface B temperature
ZFICT	Fixture interface C temperature
ZCST	Carrousel stator temperature
ZSCT1	Spectral calibration lamp 1 temperature
ZSCT2	Spectral calibration lamp 2 temperature
ZHVPST1	Detector 1 high voltage power supply temperature
ZHVPST2	Detector 2 high voltage power supply temperature
ZDT11	Detector 1 shield temperature
ZDT12	Detector 2 shield temperature
ZDRT	Digicon radiator temperature
ZOBBT	Optical bench bulkhead temperature

We next investigated the variability of the f0 term over time. Only grating 5 showed any correlation with time. Figure 10 shows the offsets (with motion from our thermal motion model removed) versus Modified Julian Date for grating 5. The correlation is not convincing but it does indicate that time variations should be monitored in the future.

A final source of motion we investigated is the detector 2 sensitivity to variations in the Earth's magnetic field (Lindler, 1991). Figure 11 shows a plot of the f0 offsets versus the geomagnetic field component in the direction of dispersion. Some correlation is evident. The slope of the least squares linear fit (shown as the solid line) is approximately 0.75 sample units per Gauss. This is consistent with other measurements of the geomagnetic sensitivity.

f1 also showed significant variations. Changes in this term represent a plate scale change. Figures 12 through 18, show the differences in the linear dispersion term from the predicted value as a percent change. The changes are plotted against the thermistor reading which gave the best correlation. A change in dispersion of 0.05 percent can result in a 0.25 sample unit error over the 500 diode array (500*0.0005). CALHRS presently has no provision for handling a thermal model of changes in the linear dispersion term. Users with observations reduced with an average dispersion coefficient table should be aware that not only is there a zero point shift in their wavelengths but also changes in dispersion.

5.0 Dispersion coefficients for arbituary carrousel positions.

The present implementation of CALHRS uses a table of dispersion coefficients tabulated on an arbitrary grid of carrousel positions. If wavelengths are required for an untabulated carrousel position, CALHRS linearly interpolates the coefficients between the two closest carrousel positions. With the significant improvements to the thermal model, this linear interpolation becomes one of the most significant remaining errors. Using the polynomial model for the dispersion coefficients from section 3.0, this error can be made negligible by creating a dispersion coefficient table on an arbitrarily small carrousel grid. We chose a grid with dispersion coefficients tabulated at every carrousel position divisible by 4. This effectively eliminated interpolation errors at the cost of substantially increasing the size of the dispersion coefficient table and thus increasing the CALHRS execution time.

6.0 CALHRS reference files

The final results of this report are tabulated in two tables for use by CALHRS. Table DC_004.TAB contains the dispersion coefficients for all grating modes, tabulated at carrousel positions divisible by 4. The coefficients were generated using the polynomial coefficients listed in table 2. A thermal coefficient table, TM_002.TAB, was generated by selecting the thermistor readings for each grating mode which gives the best correlation with spectral motion. The thermal motion coefficients in TM_002 are listed in table 3.

Table 3
Linear thermal motion coefficients

Grating	Thermistor	Motion (samples/degree)
G-1	ZDEBTR	-0.03
G-2	ZRICTA	-0.09
G-3	ZFIAT	-0.45
G-4	ZCST	-0.69
G-5	ZFIBT	0.26
E-A	ZCST	-0.37
E-B	ZDEBTR	-0.43

7.0 Errors in the wavelengths assigned by CALHRS.

There are a large number of sources which produce errors in the wavelengths generated by CALHRS. Many of the these errors can be significantly reduced by using proper observing techniques or careful reduction techniques. All errors described in this section are quoted in photocathode sample units. One sample unit equals 50 microns which is the separation between neighboring diodes.

7.1 Image motion.

The largest sources of wavelength error are thermal motion and carrousel repeatability. Table 4 gives the RMS error and the maximum error observed to date for each of the grating modes. The errors occur when performing reductions using the average dispersion coefficient table (DC_004) and no thermal motion correction.

Table 4
CALHRS errors using the average
dispersion coefficient table (DC_004)

Grating	RMS error (Sample units)	Maximum error (sample units)
G-1	.4	1.0
G-2	.5	1.3
G-3	1.6	3.3
G-4	2.0	3.7
G-5	.9	2.0
E-A	.9	1.9
E-B	.5	1.0

The errors can be reduced to those shown in table 5 by applying the simple linear thermal motion model described by TM_002.

Table 5
CALHRS errors using the average dispersion coefficient
table (DC_004) and thermal model table (TM_002)

Grating	RMS error (Sample units)	Maximum error (sample units)
G-1	.2	.4
G-2	.3	.7
G-3	.4	.9
G-4	.2	.7
G-5	.8	1.7
E-A	.2	.4
E-B	.3	.6

Thermal effects and other sources of motion errors can be further reduced by observing the spectral calibration lamp (WAVECAL) before and/or after the observation of the target. The thermal motion and carrousel repeatability errors are negligible if the WAVECAL is taken at the same carrousel position as the science observation. The only concern is for the short-term motion between the time of the spectral lamp and science observation, typically about 0.2 to 0.4 sample units/hour.

7.2 Dispersion changes.

Unlike thermally induced motion, changes in dispersion give errors in differences of wavelengths within the same observation. The linear dispersion at a carrousel position can vary by 0.1 percent. This can result in a 0.5 sample unit error when wavelengths measured at the two ends of the diode array are compared. This error can be effectively

eliminated by using the dispersion coefficients from a WAVECAL taken
before or after a science observation.

7.3 Aperture Offsets.

The wavelength offsets between the spectral calibration lamp apertures
and the small science aperture (SSA) were calibrated using prelaunch
data taken during phase 6 (1984) calibration at Ball Aerospace. The
estimated (one sigma) error in this calibration is 0.1 sample units.
There is no way for an observer to decrease this error. However, it
is important to note that the error repeats. If you observe with the
same carrousel position at two different times, the aperture offset
error is the same. A difference of two measured wavelengths from one
observation to the other will not show an aperture offset error.

The calibration between the SSA and the large science aperture (LSA)
has not yet been completed. CALHRS presently computes SSA wavelengths
for objects in the LSA. Errors resulting from this lack of
calibration are probably on the order of 1 to 2 sample units.

7.4 Target centering.

CALHRS computes wavelengths assuming that an object is centered in the
target aperture. If an object is not centered, wavelength errors will
occur. Miscentering can result from errors in the deflection
calibration, target locate or peakup, thermal or geomagnetically
induced image motion between the defcal and peakup, errors in the GHRS
onboard values for the aperture locations, errors in the slew between
the LSA and SSA, and spacecraft drift/jitter. Because of the size of
the SSA and the size of the spherically abberated stellar image the
one sigma error from miscentering in the SSA is on the order of 1/4 of
a sample unit. The best measurement of miscentering of a target in
the SSA is the comparison of the flux measurement between the LSA and
SSA: if the SSA flux is approximately 1/4 of the LSA flux, the object
is well centered. The centering error should be significantly reduced
once the new on-board SSA flux peakup routine is implemented

7.5 Geomagnetic image motion.

The detector 2 sensitivity to the Earth's magnetic field can result in
loss of spectral resolution and wavelengths errors up to 0.5 sample
units. To avoid loss of spectral resolution, detector 2 spectral
observations should be limited to short exposures (i.e. 5 minutes or
less). If it is found that the detectors sensitivity to the Earth's
magnetic field does not vary, it will be easy to model the geomagnetic
motion and remove it. If the sensitivity does vary (as shown to be
the case for the Faint Object Spectrograph). a WAVECAL taken before
and after the science observation could be used to calibrate the
sensitivity value at the time of the science observation.

7.6 The dispersion model.

Dispersion coefficients are computed by least squares fits of the dispersion model to spectral line positions measured in spectral calibration lamp observations. A measure of the errors in the dispersion coefficients is the RMS of the differences between the observed spectral line positions and the positions computed by the dispersion model. We found typical RMS errors of 0.04-0.08 sample units for the first order gratings and 0.1-0.15 sample units for the echelle modes. The RMS errors in the echelle modes are slightly larger because of the inadequacies in the dispersion model when the entire format (multiple spectral orders) was fit simulataneously. The RMS residuals for the echelle modes can be reduced to less than 0.1 when single orders are fit.

8.0 Ultimate wavelength precision.

If proper observing techniques are used, what is the ultimate wavelength precision of the GHRS? If WAVECALs are taken before and after the science observation in the SSA, errors from image motion, carrousel repeatability, and geomagnetic motion can be rendered negligible. The remaining errors are:

1) Errors in the dispersion coefficients (0.1 sample units)
2) Errors in the wavelength offsets between the spectral calibration lamp and small science aperture (0.1 sample units)
3) Errors caused by improper centering of the object in the SSA

With the present state of instrument calibration, errors in the centering can result in wavelength errors of approximately 0.25 sample units (one sigma). Once the SSA flux peakup option becomes available, this error will probably be reduced to approximately 0.1 sample units (one sigma). Combining these three sources of errors (0.1, 0.1, and 0.1) gives the residual error of 0.17 (the square root of [3 x 0.1 squared]) which equals approximately 0.5 km/s in the echelle modes.

REFERENCES

Cushman, G., Ebbets, D., and Holmes, A., 1986,PRE-LAUNCH CALIBRATION REPORT FOR THE HIGH RESOLUTION SPECTROGRAPH FOR THE HUBBLE SPACE TELESCOPE, Ball Aerospace, HRS-2176-051 pp. 10-5 to 10-21.

Lindler D. J. 1991 GHRS Geomagnetic Image Motion, GHRS-SV-

Reader, J., Acquista, N., Sansonetti, C. and Sansonetti, J., 1990, Wavelengths and Intensities of a Platinum/Neon Hollow Cathode Lamp in the Region 1100-4000 Angstroms, The Astrophysical Journal Supplement Series. 72:831-866, 1990 April.

Figure Captions

figure 1: Wavelength calibration residuals of the observed grating 2 spectral line positions from those of least squares quadratic dispersion model. Residuals are in 50 micron sample units. The plot shows the need for a cubic dispersion term.

figure 2: Same as figure 1 except that a cubic dispersion model was used.

figures 3-9: Linear thermal motion models for each grating. The plus marks (+) show the offset of each spectral lamp observation from an average dispersion model for the grating plotted against the GHRS thermistor value with the best correlation. The solid lines are linear least squares fits. Offsets are in 50 micron sample units and temperatures are in degrees Celsius.

figure 10: Grating 5 spectral motion with time. The plus marks (+) show the offset of each spectral lamp observation from an average dispersion model for the grating plotted against time. The solid line is a linear least squares fits. Offsets are in 50 micron sample units.

figure 11: Detector 2 spectral motion plotted against the conponent of the Earths magnetic field in the dispersion direction. The plus marks (+) show the offset of each grating 2, 3 or 4 spectral lamp observation from an average dispersion model for the grating. The solid line ia a linear least squares fits. Offsets are in 50 micron sample units.

figures 12-18: Changes in the linear dispersion with temperature. The plus marks (+) show the change of the dispersion for each individual spectral calibration lamp observation from an average dispersion model for the grating. The solid line shows a the least sqaures fit of the changes with the GHRS thermistor giving the best correlation with temperature. The temperatures are plotted in degrees Celsius.

Figure 1

G-2 Quadratic Fit
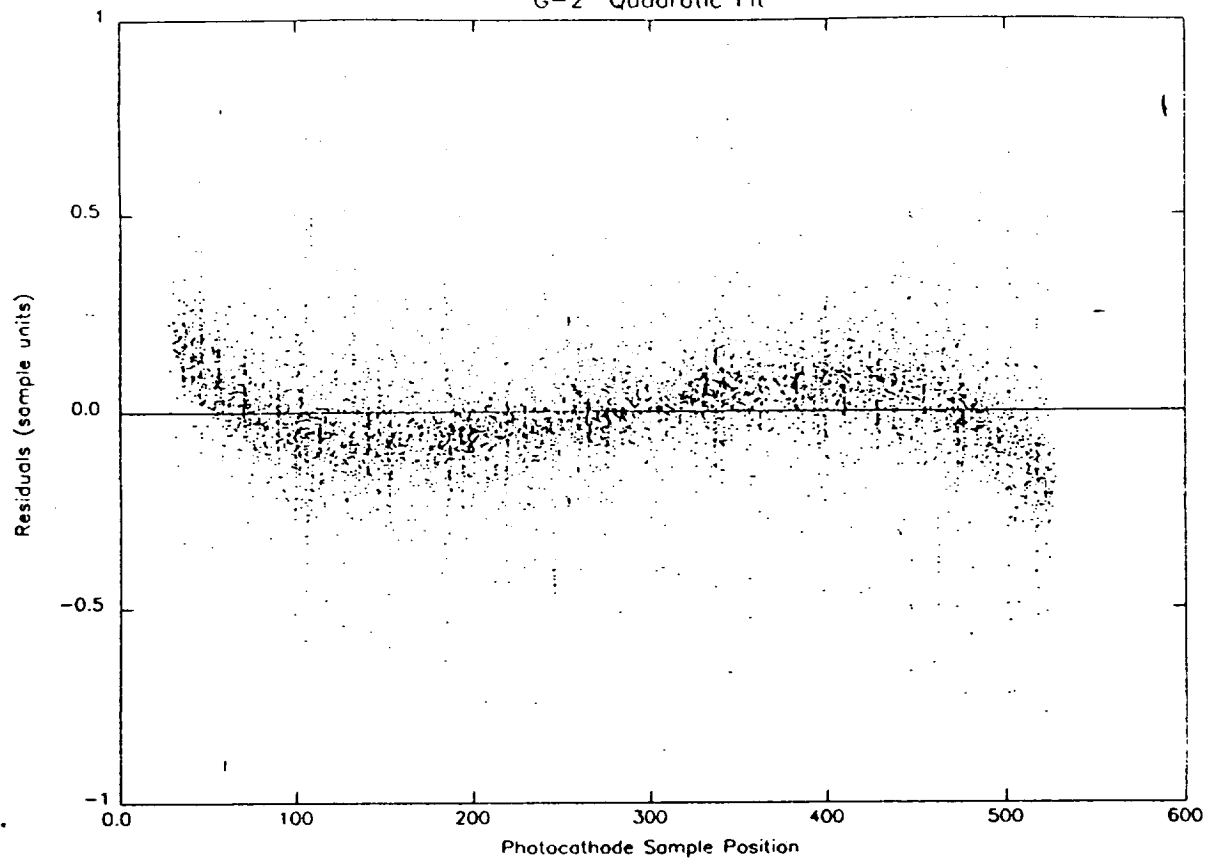
Figure 2

G-2 Cubic Fit
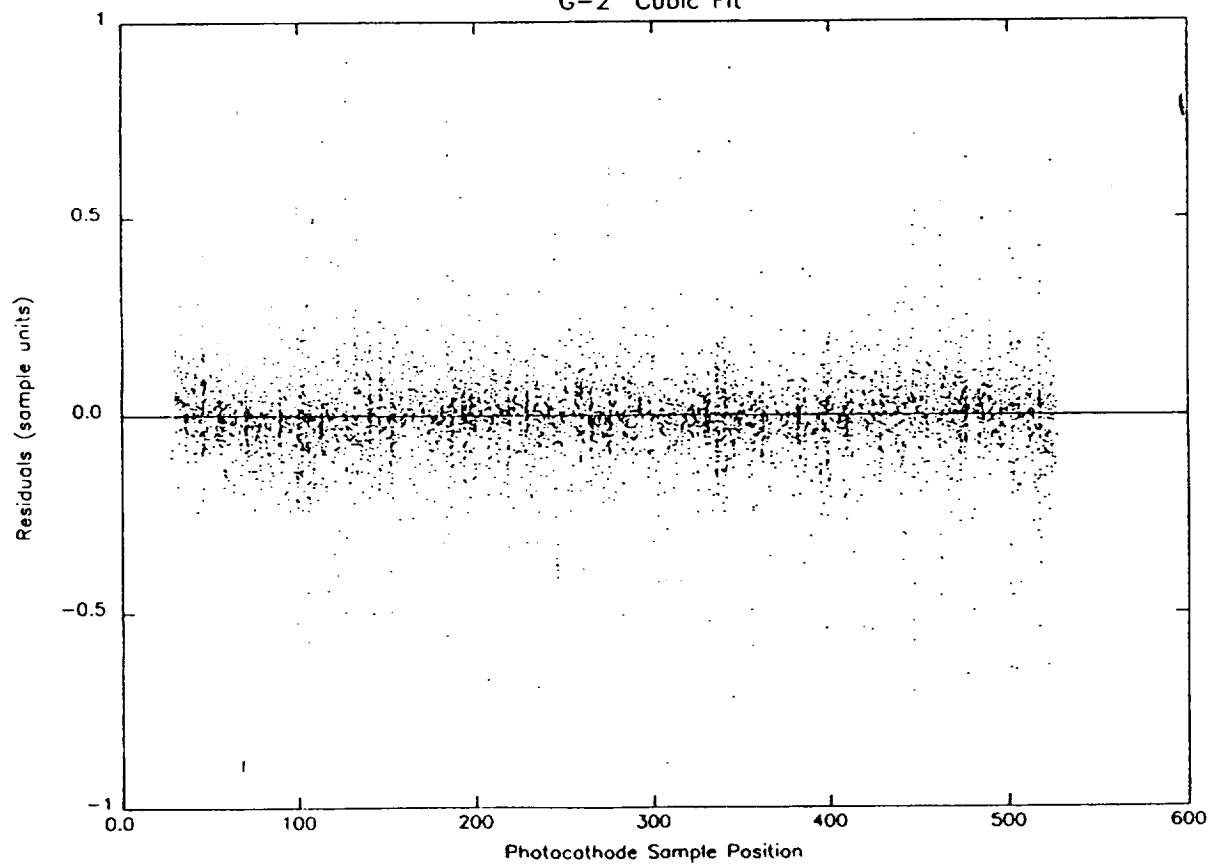
Figure 3
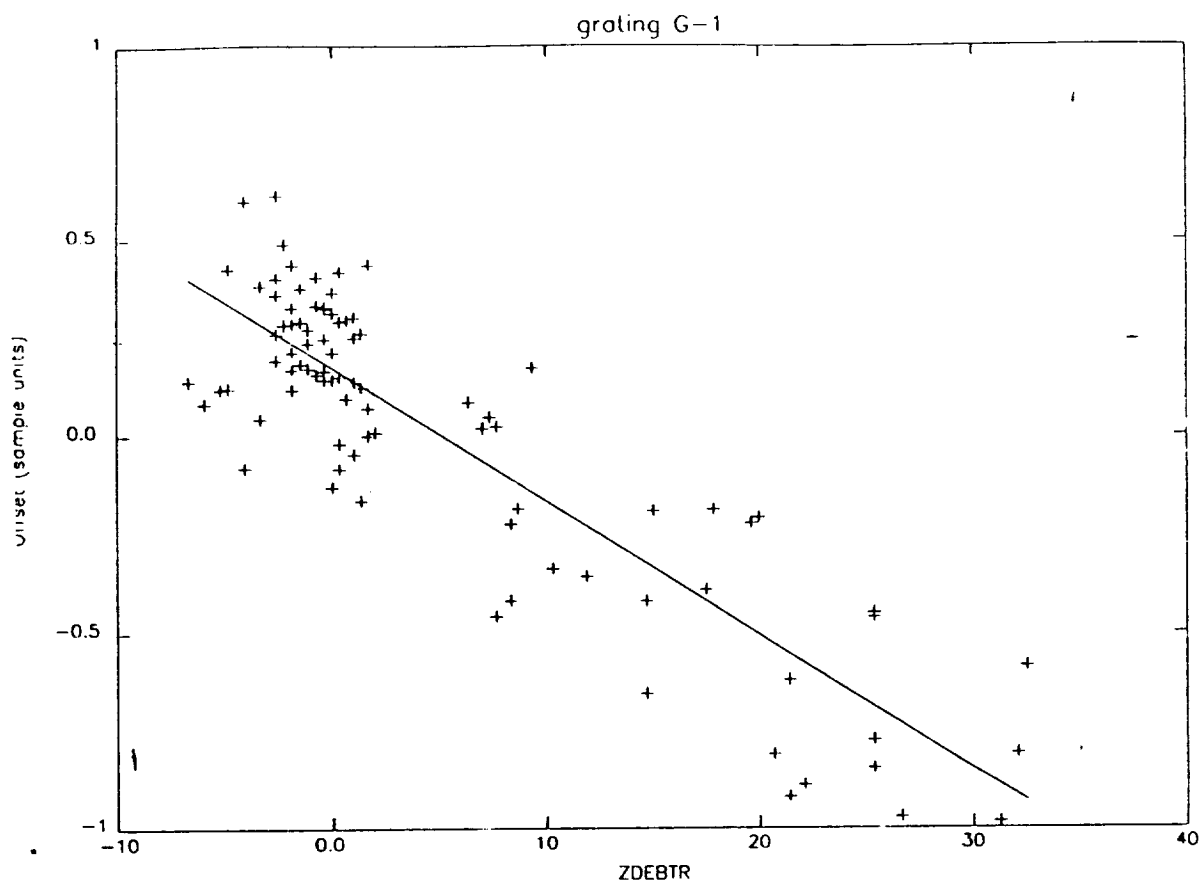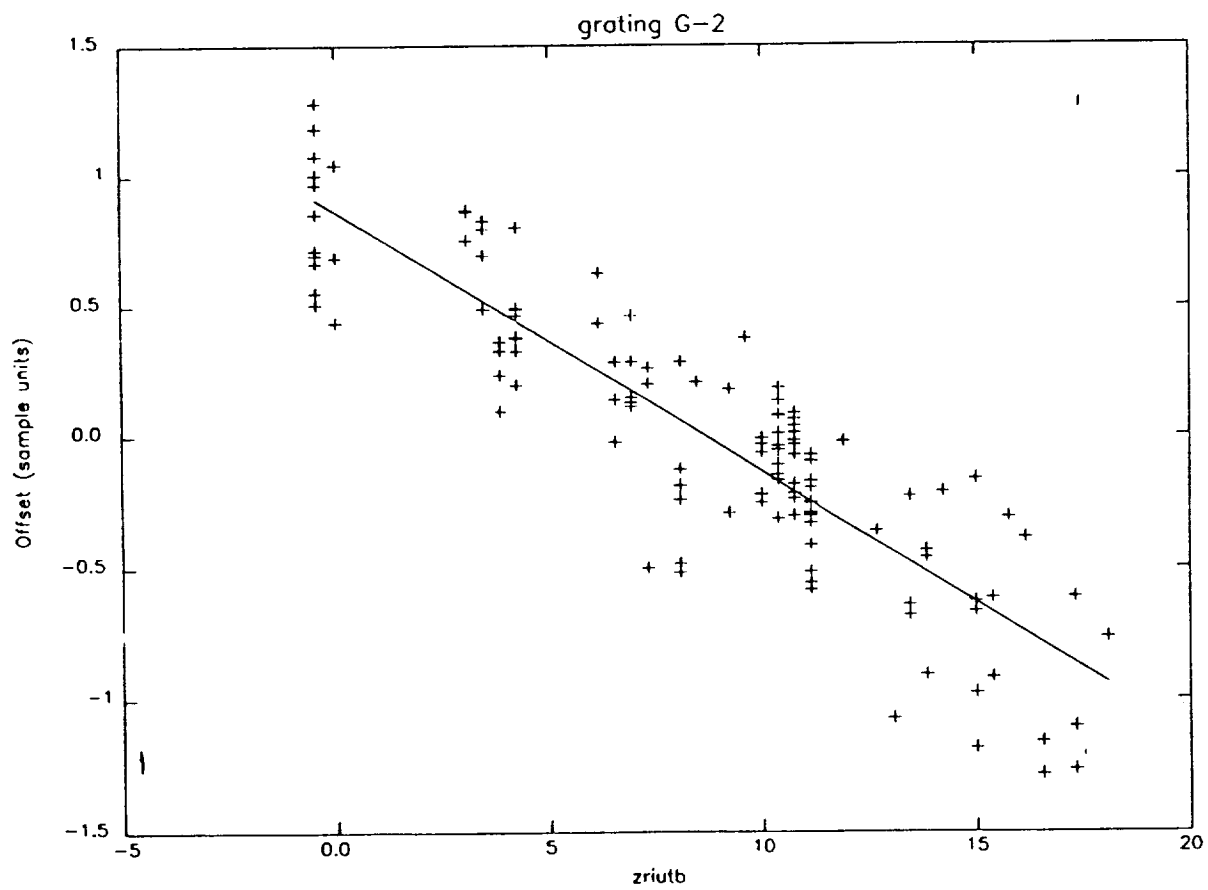
grating G-1

Figure 4

grating G-2

Figure 5

grating G-3
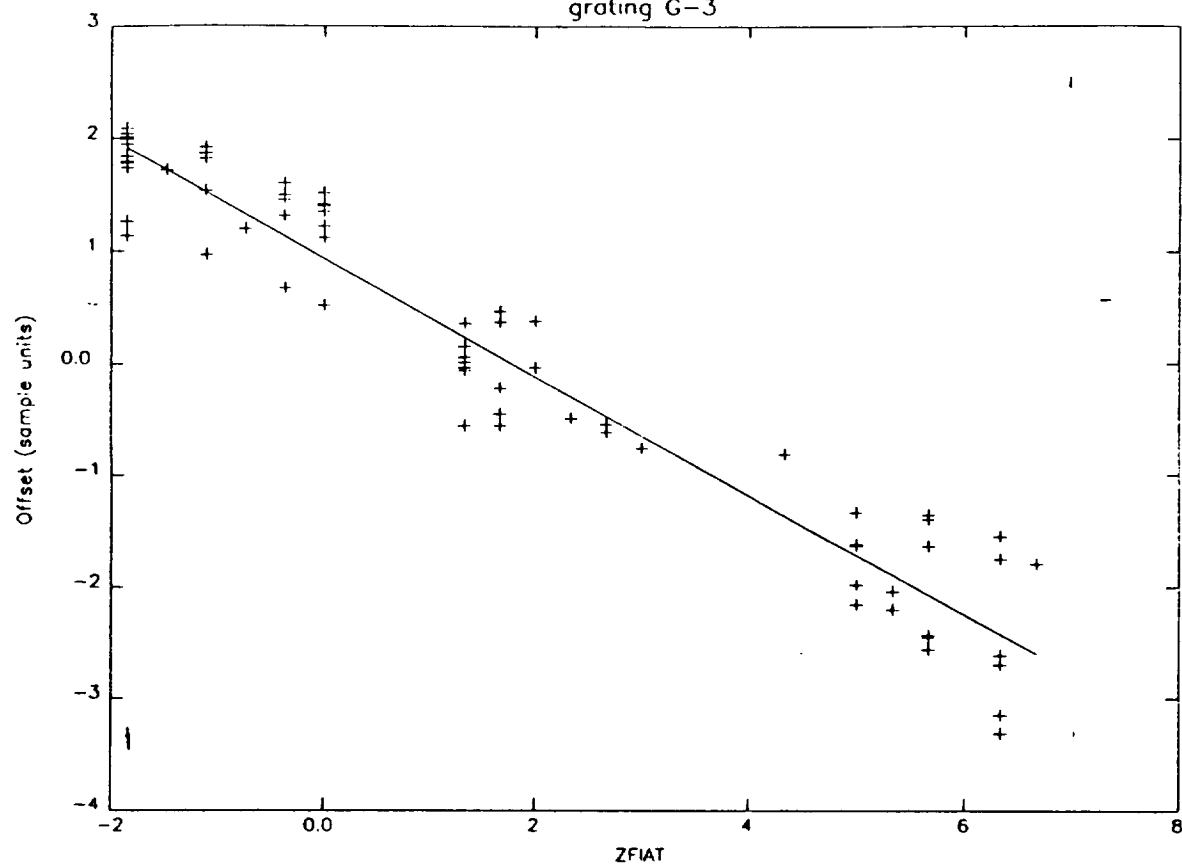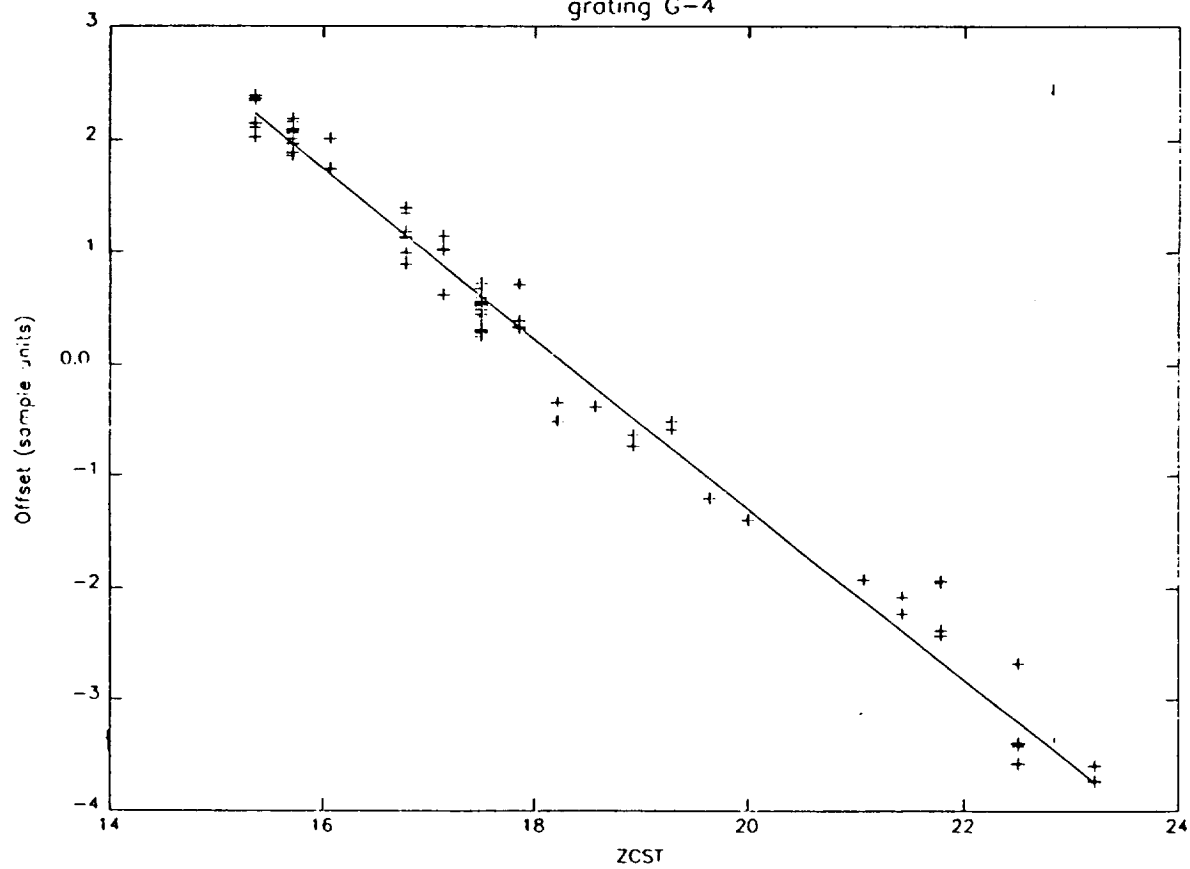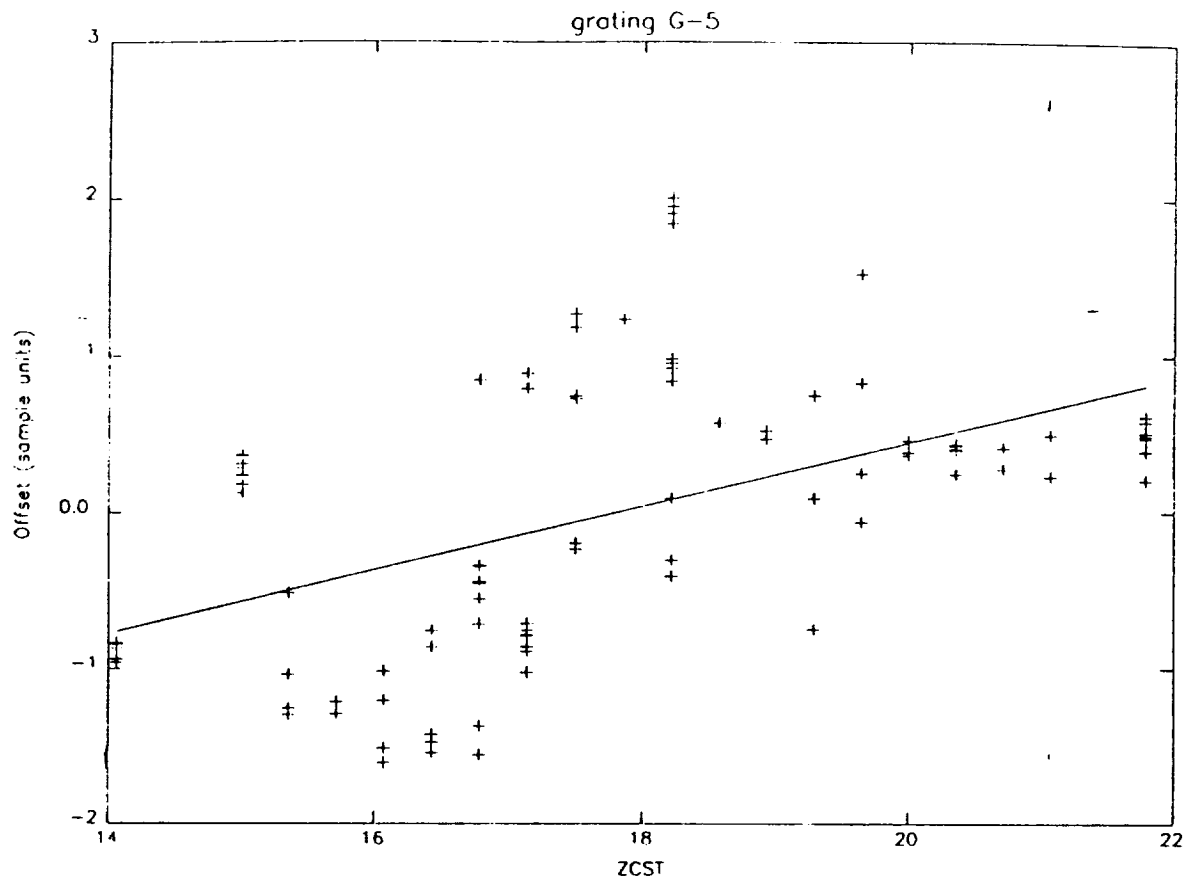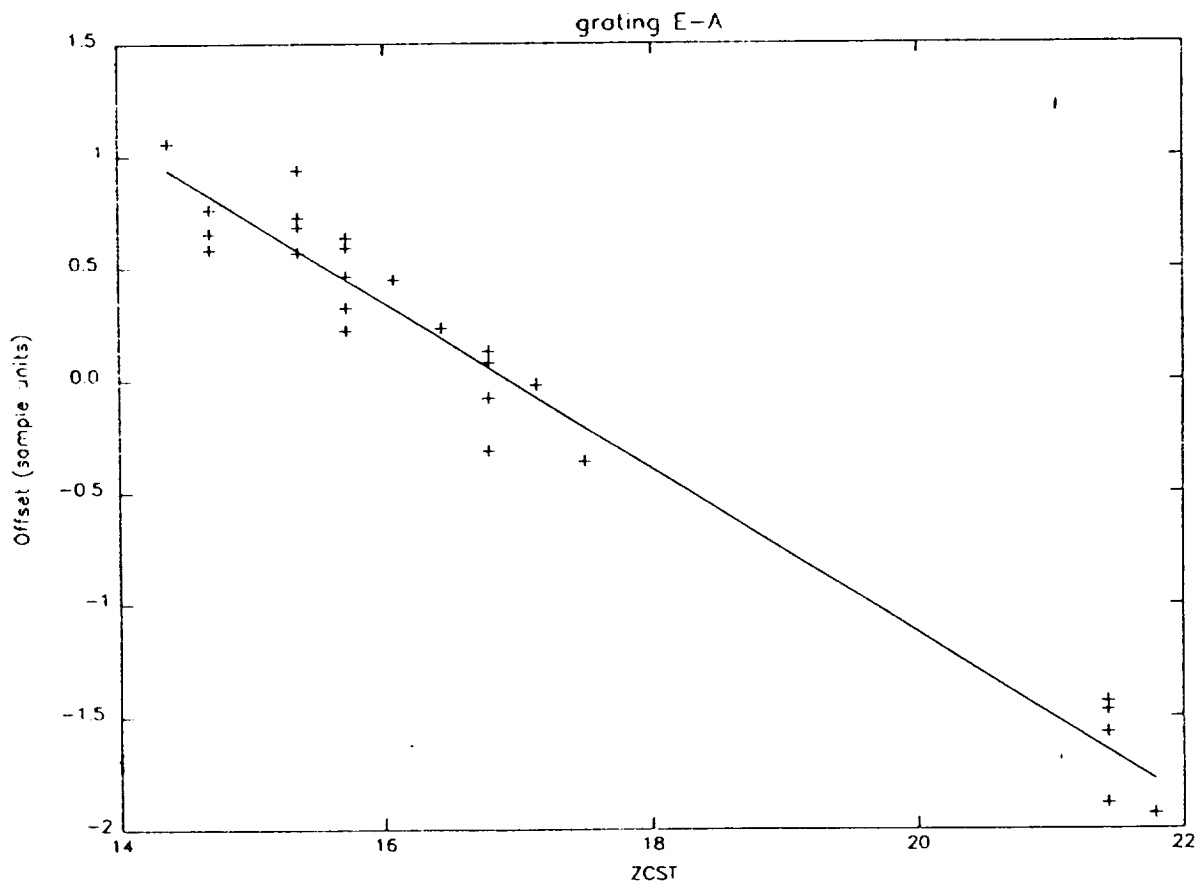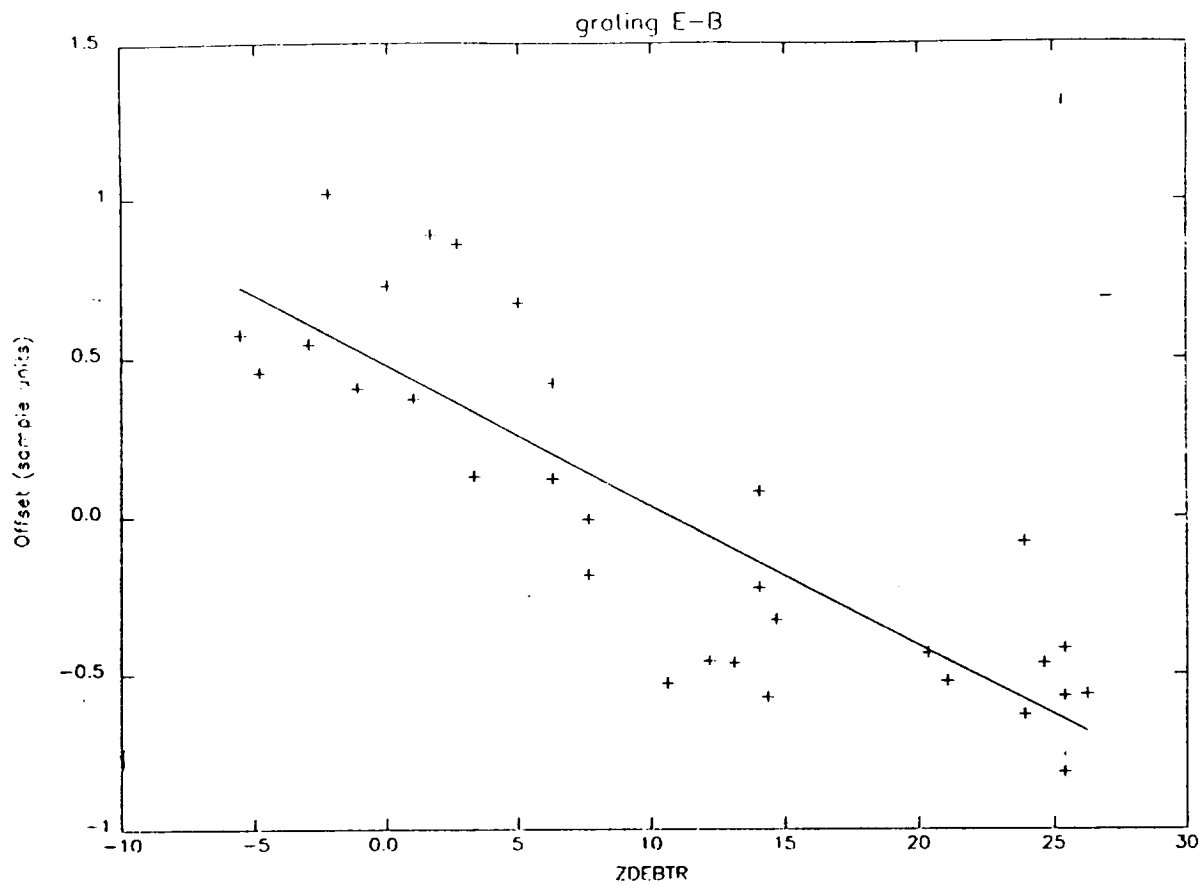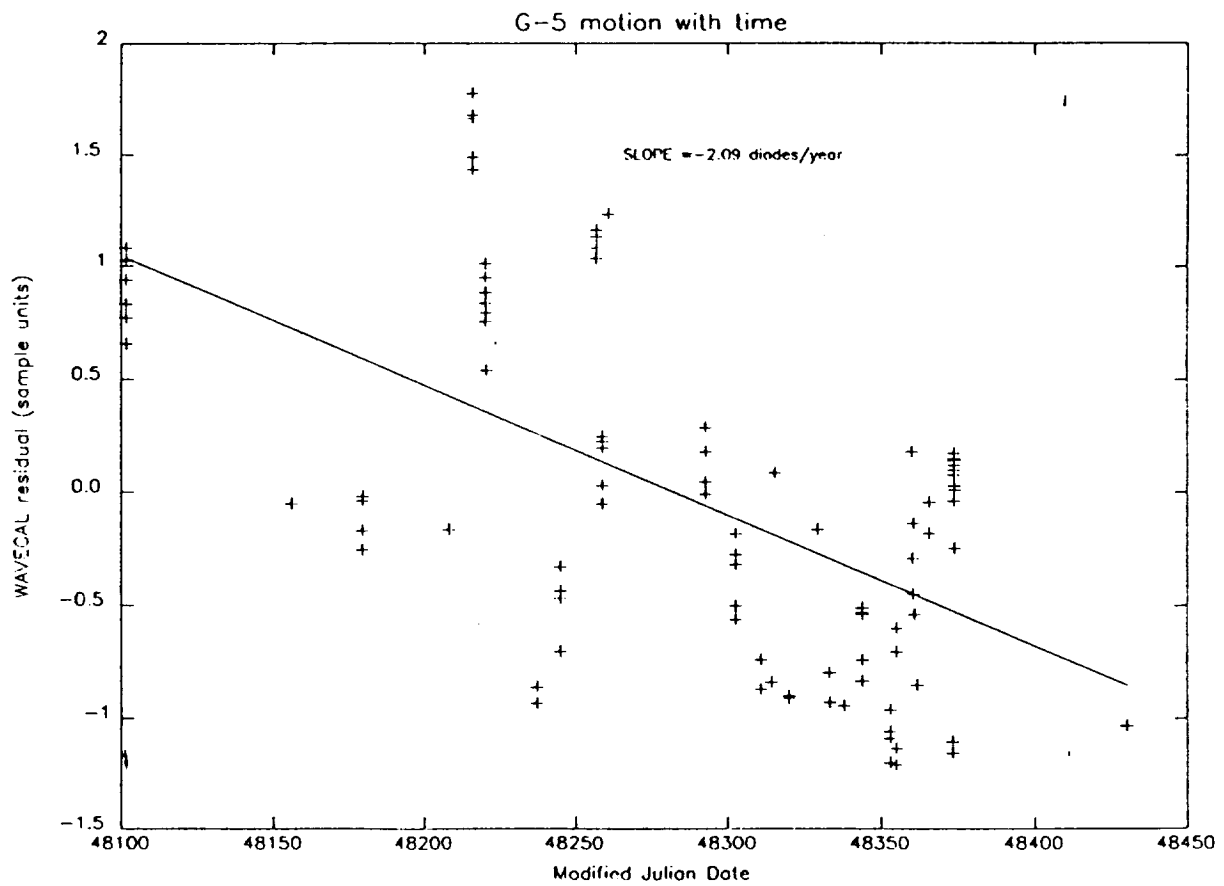
Offset (sample units) vs ZFIAT

Figure 6

grating G-4

Offset (sample units) vs ZCST

Figure 7

grating G-5

Figure 8

grating E-A

Figure 9

groting E-B

Figure 10

G-5 motion with time

Figure 11

Detector 2 Geomagnetic Image Motion

Figure 12

grating G-1

Figure 13

grating G-2

Figure 14

grating G-3

Figure 15

groting G-4

Figure 16

groting G-5

Figure 17

grating E-A

Figure 18

grating E-B
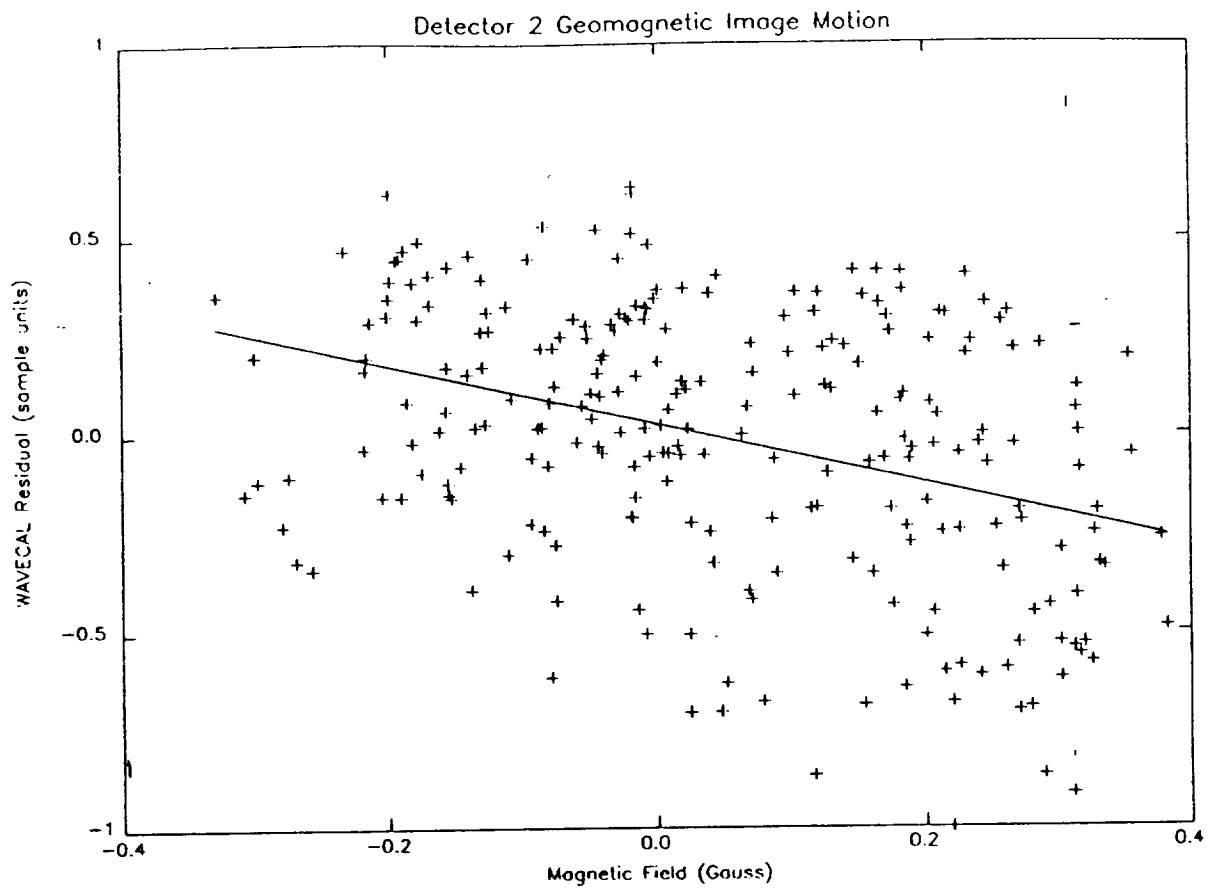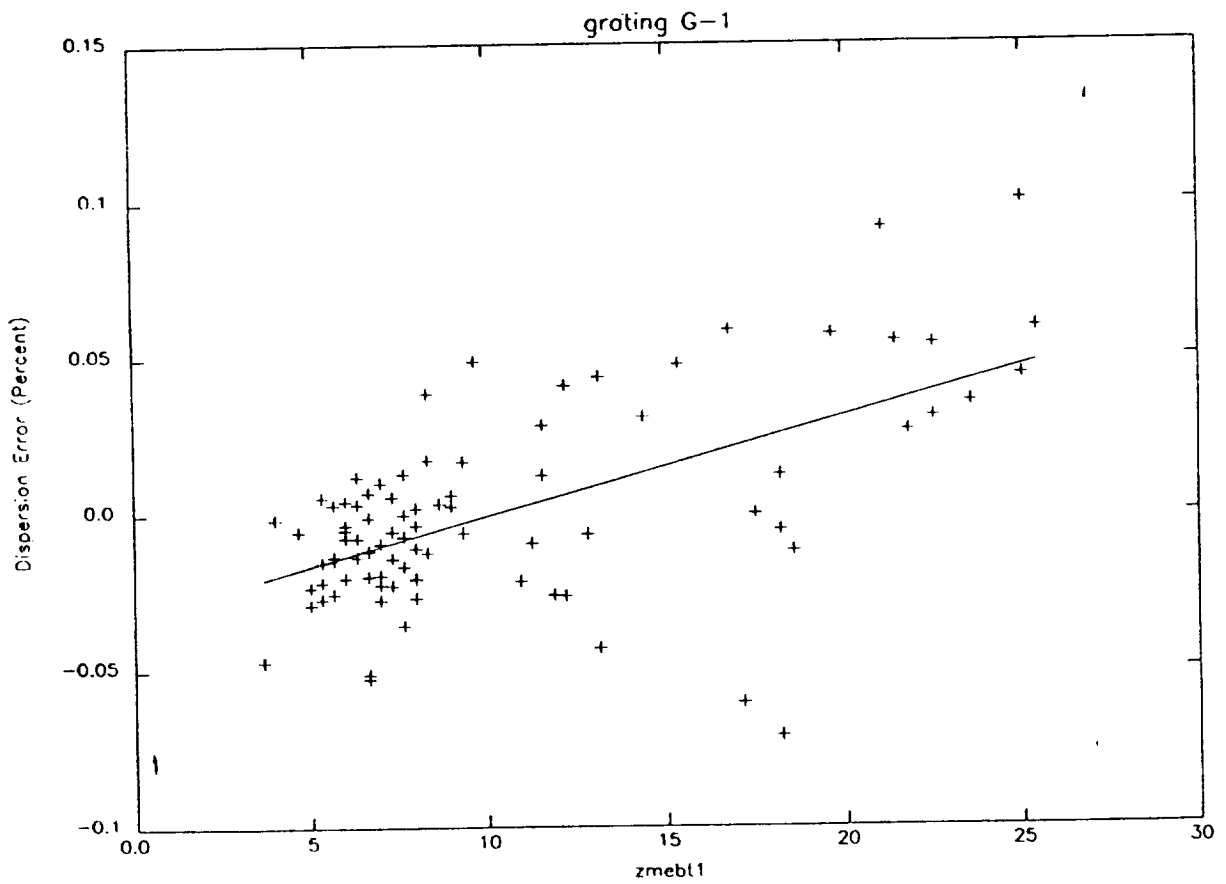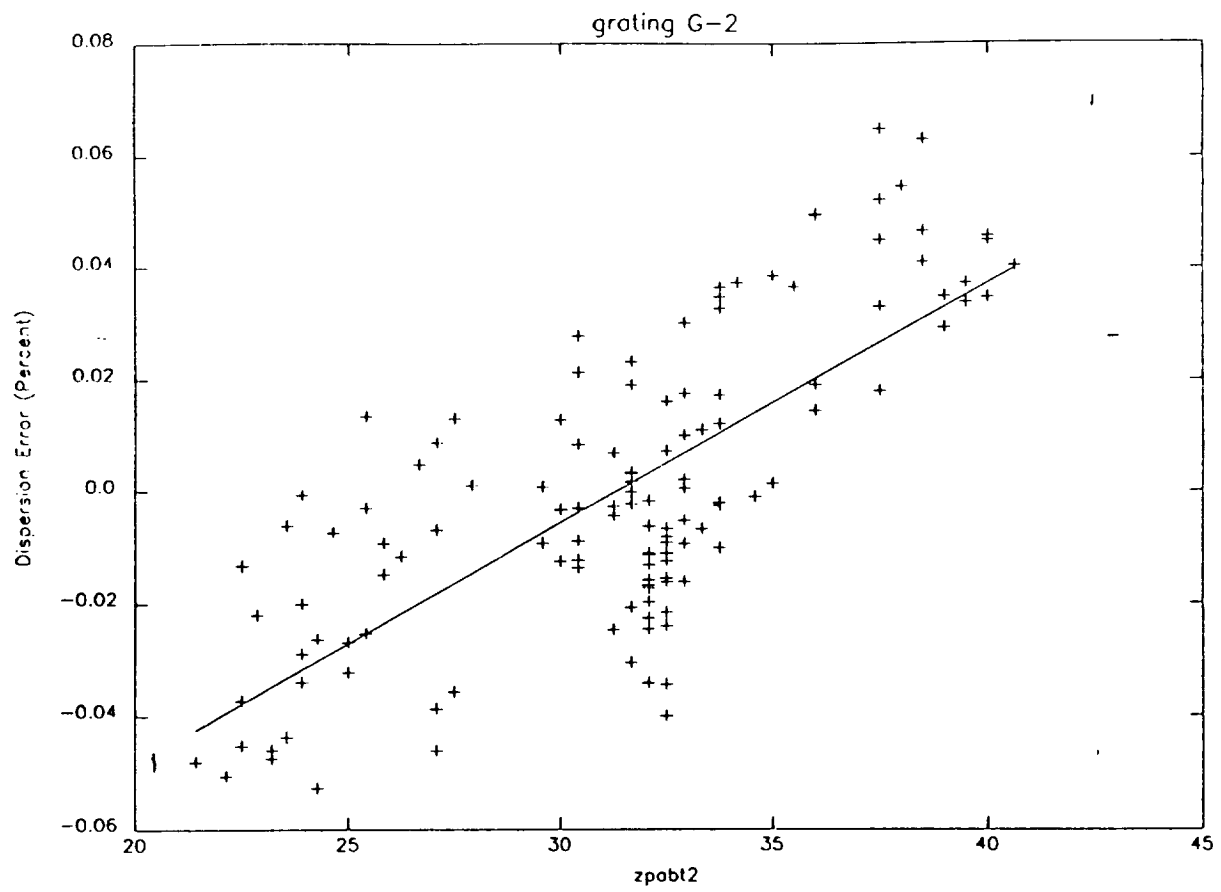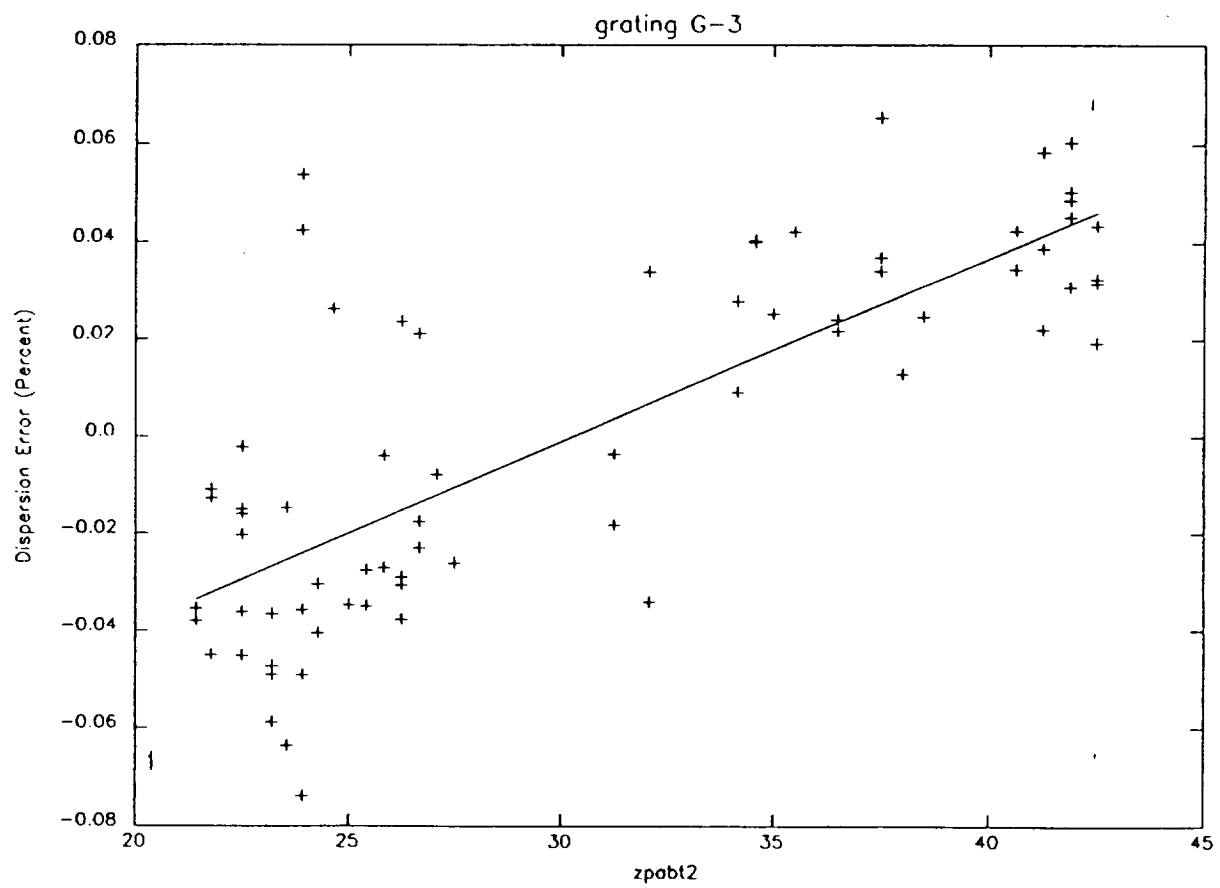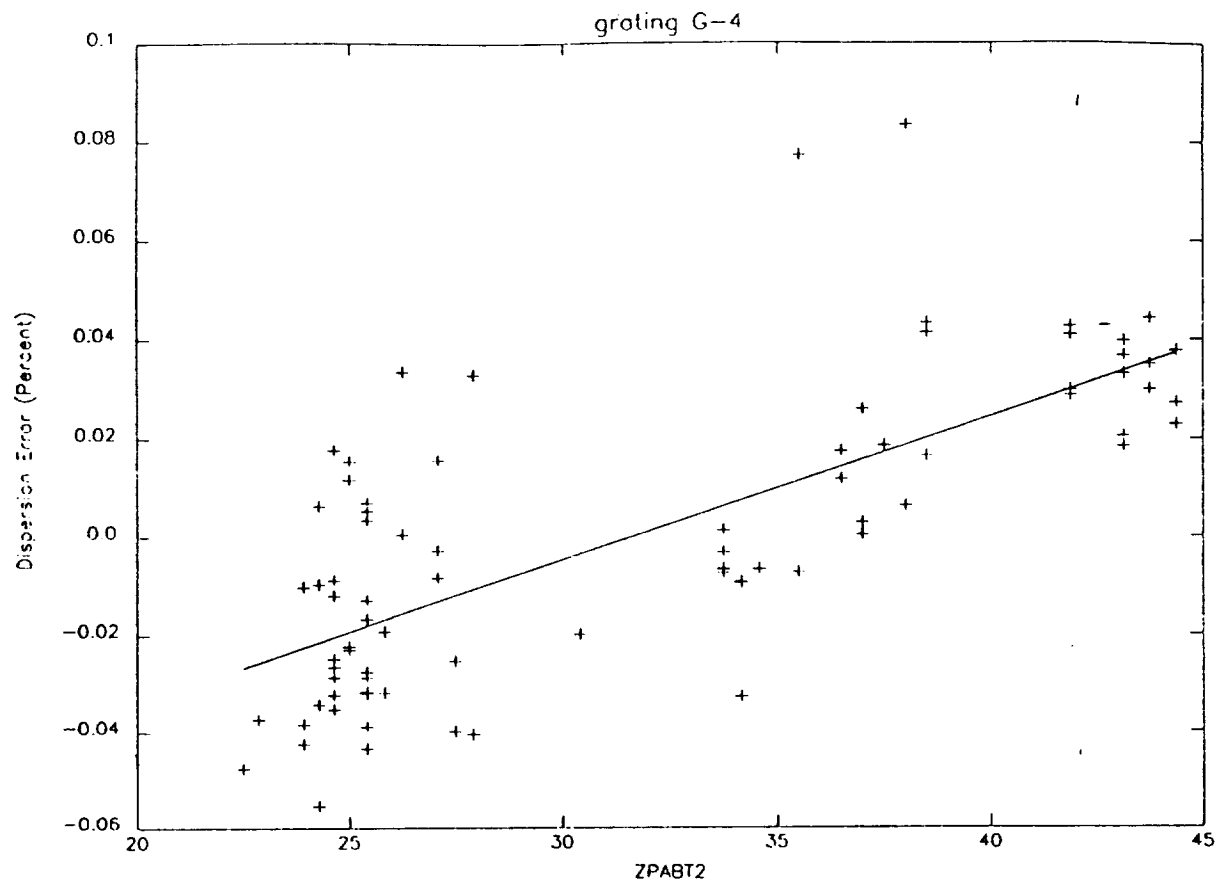
GHRS Wavelength Offsets Between the Large and
Small Science Apertures.

Don Lindler
October 30, 1991

ABSTRACT

We have made measurements of the offsets between the large (LSA) and
small (SSA) science apertures for GHRS gratings 2, 3, and 4. In all
cases the measured offsets were less than one diode and the average
offset for each grating mode was less than 1/2 diode. There was
insufficient data to quantify changes in the offsets versus carrousel
position and photocathode sample positions. However, grating 2
results indicate that the offset does vary with carrousel position.

1) INTRODUCTION

The standard GHRS reduction routine, CALHRS, has the provision for
applying a wavelength offset to the wavelengths computed from a table
dispersion coefficients. The dispersion coefficients are used to
compute wavelengths applicable to data taken in the small science
aperture. The wavelength offsets for the other apertures are computed
by:

$$DW = (A + B*s)/m \tag{1}$$

where,

> DW is the offset added to the small science aperture
> wavelength values.

> s is the photocathode sample position of the data point.

> m is the spectral order (1 for the first order gratings)

> A and B are offset coefficients that are tabulated by grating
> mode, aperture, spectral order, and carrousel
> position.

Prelaunch measurements of the offsets between the small science
aperture and the spectral calibration lamp apertures (SC1 and SC2)
show variations in A and B for changes in both carrousel position and
spectral orders. Results also show that B is non-zero. This means
that not only is there a wavelength offset between entrance apertures

but there is also a plate scale change.

Measurements of the offsets between the SSA and the spectral calibration lamp apertures were made in 1984 by illuminating the SSA with a platinum/neon spectral calibration lamp. No measurements of the offsets between the SSA and LSA were made during the prelaunch calibration.

Data for measurement of the offsets between the SSA and LSA were taken on June 15, 1991 (proposal 2097). The data consisted of observations of HD93521 taken in both the large and small science apertures. Prior to each observation, wavelength calibration observations were taken so that any effects of thermal motion, geomagnetic induced motion, and carrousel repeatability could be removed. Five carrousel positions were observed for grating 2 and three carrousel positions were observed for gratings 3 and 4.

2) DATA REDUCTION

For each carrousel position the following sequence of observations was made.

    A) Spectrum Y-Balance observation
    B) Wavecal observation using lamp SC1
    C) HD93521 observation through the LSA
    D) Spectrum Y-Balance observation
    E) Wavecal observation using lamp SC1
    F) HD93521 observation through the SSA

Observations B and E were used to remove any of the wavelength offsets between observations C and F which resulted from thermal and geomagnetic image motion or from the carrousel motion needed for the spectrum Y-balance observations. The offsets between observations B and E and observations C and F were computed using a normalized mean and variance correlation. Quadratic refinement of the correlation values was used to determine the offset to sub-pixel accuracy. Observations C and D were smoothed to the same resolution before correlation by convolving the LSA observation with the SSA line spread function and the SSA observation with the LSA line spread functions. To minimize the effect of fixed pattern noise, the correlations of HD93521 were limited to regions with large spectral features.

The offset between the SSA and LSA was then computed as the offset between observation C and F minus the offset between observations B and E.

3) ANALYSIS

The offsets that we computed between the SSA and LSA are tabulated in table 1 versus grating mode, carrousel position, and photocathode sample position. The photocathode sample position column gives the position of the center of the HD93521 spectral feature that was correlated.

The results for grating 2 show some evidence that the offsets vary with carrousel position. The grating 2 observations at carrousel position 51508 also show some evidence that the offset also varies with sample position. Variations with sample position would indicate that the plate scale or dispersion is different between the two apertures.

To implement the LSA/SSA offset correction in CALHRS, we have elected to only use an average offset for each grating. The minimal amount of data does not allow us to construct accurate models of the variations of the offset with carrousel position and sample position. The resulting coefficients (Equation 1) for use by CALHRS are then:

Grating	A	B
G-2	-0.022	0.0
G-3	-0.037	0.0
G-4	-0.036	0.0

It should be noted that there may be errors in these coefficients resulting from the target acquisition of HD93521 in the LSA and SSA. These errors include; statistical errors in the on-board deflection calibration and LSA locate, errors in the calibrated position of the LSA with respect to the calibration lamp apertures, and errors in the slew between the LSA and SSA. No peakup was performed to center the object in the SSA.

TABLE 1

Wavelength Offsets Between the
Large and Small Science Apertures

Grating	Carrousel Position	Photocathode Sample Positon	Offset (diodes)	Offset (Angstroms)
G-2	49936	244.	0.82	0.058
G-2	50680	229.	0.48	0.034
G-2	51096	164.	0.70	0.050
G-2	51096	292.	0.44	0.031
G-2	51304	417.	0.55	0.039
G-2	51508	85.	-0.08	-0.005
G-2	51508	160.	-0.09	-0.006
G-2	51508	273.	0.04	0.003
G-2	51508	323.	0.17	0.012
G-2	51508	404.	0.09	0.007
G-3	25056	335.	0.38	0.030
G-3	25876	354.	0.59	0.046
G-3	26288	276.	0.31	0.024
G-3	26288	367.	0.63	0.049
G-4	9360	242.	0.46	0.042
G-4	9360	317.	0.44	0.040
G-4	9832	235.	0.25	0.022
G-4	9832	339.	0.41	0.037
G-4	9832	395.	0.35	0.031
G-4	9832	483.	0.44	0.040
G-4	10256	223.	0.48	0.043
G-4	10256	311.	0.39	0.035

BLOCK ITERATIVE RESTORATION OF ASTRONOMICAL IMAGES FROM THE HUBBLE SPACE TELESCOPE

Don J. Lindler

Advanced Computer Concepts
Potomac, Maryland

1. INTRODUCTION

The discrete model of linear image degradation is specified by the equation:

$$\mathbf{b} = H\mathbf{x} + \mathbf{n} \tag{1}$$

where b and x are the pixel values of the degraded and original undegraded images stacked into column vectors, H is a matrix constructed from the impulse response (or point spread function) of the degradation, and n is an unknown additive noise vector. The object of restoration is to determine x, given b and possibly information on the properties of n. If the point spread function used to construct H is not known for the given optical- detector configuration, it must be estimated from the blurred image, b. The point spread function is most easily estimated from point sources (*i.e.* stars) on the blurred image.

Since H may be ill-conditioned or singular, and only the statistical properties of the noise are known, there are many solutions for x which satisfy equation (1). The success of a restoration therefore depends on the ability to model and apply to the restoration, known or assumed properties of the desired solution, such as positivity or smoothness.

Some advantages of algebraic image restoration are:
1) The point spread function may be spatially variant;
2) If a constrained least squares method is used, the applied constraints may be varied from pixel to pixel to make maximum use of the known image properties;
3) Missing or bad pixel values in the blurred images can be easily handled without attempting to repair their values;
4) Noise properties can vary from pixel to pixel.

The main disadvantage of algebraic image restoration is the size of the linear system. For a 500×500 pixel image, H is a $250,000 \times 250,000$ matrix. Even with the most powerful computers available, a direct solution of the system would be impossible. In the next section, we describe a technique – the block iterative method, of solving large linear systems.

2. THE BLOCK ITERATIVE RESTORATION ALGORITHM

2.1 Block Jacobi Iteration

In most astronomical images, the point spread function has a much smaller spatial extent than the image, so it is appropriate to work on the image locally. We therefore divide the image into blocks and restore each block separately, using values from the previous iteration as estimates of the unblurred image values outside the block. In most instances the blurred image

is a good choice for the starting or zeroth iteration. This type of iteration is called block Jacobi or group Jacobi iteration (Young 1971) and can be formulated in matrix notation as follows.

Consider the blurred image, b, divided into m blocks of equal size B_i, i = 1,m:

$$B = \begin{pmatrix} B_1 & B_2 & \cdots & \cdots \\ & B_{i-1} & B_i & B_{i+1} \\ & \cdots & & \\ & & B_{m-1} & B_m \end{pmatrix}$$

Stack the elements of each block and place them into a vector:

$$\mathbf{B} = (B_1, B_2, \cdots, B_m)^T$$

Ignoring the noise for now, we write the system as:

$$H\mathbf{X} = \mathbf{B}$$

where H is partitioned into blocks

$$H = \begin{pmatrix} H_{11} & H_{12} & \cdots & H_{1m} \\ H_{21} & H_{22} & \cdots & H_{2m} \\ & \cdots & & \\ H_{m1} & H_{m2} & \cdots & H_{mm} \end{pmatrix}$$

and $\mathbf{X}$ contains the restored values, blocked in the same manner as $\mathbf{B}$. If the image were divided into blocks of n pixels each, then the block H_{ij} would have size $n \times n$. The block Jacobi method can now be written as:

$$H_{ii}X_i^{r+1} = B_i - \sum_{j=1, j \neq i}^{m} H_{ij}X_j^r \tag{2}$$

$i = 1, \cdots, m$, and where X_i^r is the stacked values for iteration r of block j. If we define the vector on the right hand side of equation (2) as $BMOD_i$ (i.e., the blurred image less contributions from outside the block as estimated from the previous iteration), the linear system for block i can now be written as:

$$H_{ii}X^{r+1} = BMOD_i \tag{3}$$

Using the block Jacobi method, we can reduce the problem to solving

$$H\mathbf{x} = \mathbf{b} \tag{4}$$

where H is H_{ii} for block i; $\mathbf{x}$ is X_i^{r+1} for block i and iteration r; and $\mathbf{b}$ is $BMOD_i$ for block i.

The solution for block i now requires the solution of an $n \times n$ linear system. For example, to restore a 100×100 pixel image divided into m=100 blocks, each of size $n \times n = 10 \times 10$, the largest system to be solved would have H_{ii} of size 100×100. Since solutions of linear systems require on the order of n^3 operations, the block approach compares favorably to the direct solution of the $10,000 \times 10,000$ system. For a spatially invariant point spread function, the problem is further reduced because H_{ii} will be identical for all $i = 1, \cdots, m$.

If a constrained least squares approach is used to solve the linear system, the solution will converge to acceptable results even with a block size as small as the full-width-at- half-maximum (FWHM) of the point spread function. Overlapping the blocks (accepting only the central portion for the next iteration) can be used to speed convergence.

2.2 Image Constraints

The block Jacobi method reduces the restoration to solution of many smaller linear systems, but it does not address the ill-conditioned nature of H or the presence of noise in the blurred image. An ill- conditioned matrix means small changes in **b**, caused by noise, yield large changes in the solution $x = H^{-1}b$. In this section, we show how constrained solutions can handle these problems.

In most images, the data vary smoothly except at isolated points or edges. For example, an image of a star field will vary smoothly, except at locations of individual stars. We can make use of this image properly, smoothness, by applying a constrained least squares fit. Specifically, we minimize a linear operator $\|Qx\|$ (*i.e.* the sum of the squares in Qx), where Q is a matrix designed to control smoothness or other characteristics of the image (Twomey 1963, Philips 1962). For example, we can control smoothness in the one dimensional case by minimizing the second difference in the solution subject to some other constraint. If the statistical properties of the noise are known, we could minimize the second difference such that the norm of $\|Hx - b\| =$ n; that is to say, the difference of the blurred image and the solution reconvolved with the point spread function should have the same properties as the noise. In this case (minimize the second difference), Q would have the form:

$$
Q = \begin{pmatrix}
0 & 0 & & & \\
-1 & 2 & -1 & & \\
& -1 & 2 & 1 & 0 \\
& & -1 & 2 & -1 \\
& & & 0 & 0
\end{pmatrix}
$$

We use the method of Lagrangian multipliers, sometimes called the method of undetermined multipliers, to compute a solution, **x**, given by (Andrews 1977):

$$
x = (H^T H + \gamma Q^T Q)^{-1} H^T b \tag{5}
$$

γ is the reciprocal Lagrangian multiplier which can be selected to control the smoothness of the solution. Solutions using Lagrangian multipliers place no restrictions on the form of Q. This flexibility allows the development of a variety of constraints depending on the known properties of the image.

Figure 1 shows the application of this constrained least squares filter for a test case (a point source) with different values of γ_2. The subscript 2 is used to indicate that the constraint is the minimum second difference. Note in figure 1.c, with the largest value of γ_2, noise in the solution has been supressed. However, the width of the point-source profile is almost as wide as the blurred profile. Also, some ringing in the restored profile is evident. Restored values on each side of the profile drop significantly below the background level. These problems result

because the second difference is large at the location of a point source. We therefore remove the second-difference constraint at the point source by setting the rows of Q corresponding to the point-source location to zero. Figure 1.f shows a restoration of the same test image when the second difference constraint is not applied at the point source. A significant improvement is apparent.

A direct extension of the method to two dimensional images is to minimize the Laplacian at each point. The Laplacian operator has a value at each pixel equal to four times the pixel value minus the values of the four immediate neighboring pixels. We use the subscript, L, to indicate the presence of the Laplacian constraint. As before, we set rows of the matrix Q to zero when the Laplacian constraint is not appropriate (i.e. edges or point sources).

The constraint need not be binary: we can vary the amount of constraint between no constraint to full constraint for any pixel, simply by multiplying the appropriate row in Q by a constant factor running from 0 to 1.

Another useful constraint is to minimize the difference of x from a trial solution (i.e. minimize $\|p - x\|$). The solution using Lagrangian multipliers is given by (Twomey 1963):

$$x = (H^T H + \gamma_t I)^{-1}(H^T b + \gamma_t p) \quad (6)$$

where p is the trial solution, I is the identity matrix, and γ_t is the reciprocal Lagrangian multiplier. The subscript, t, will be used to identify the constraint as minimization of the solution from a trial solution. Some possible choices for the trial solution, p, are a constant value (i.e. all zeros) or the blurred image itself. In either case, the ill-conditioned nature of H can be avoided and reasonable solutions obtained.
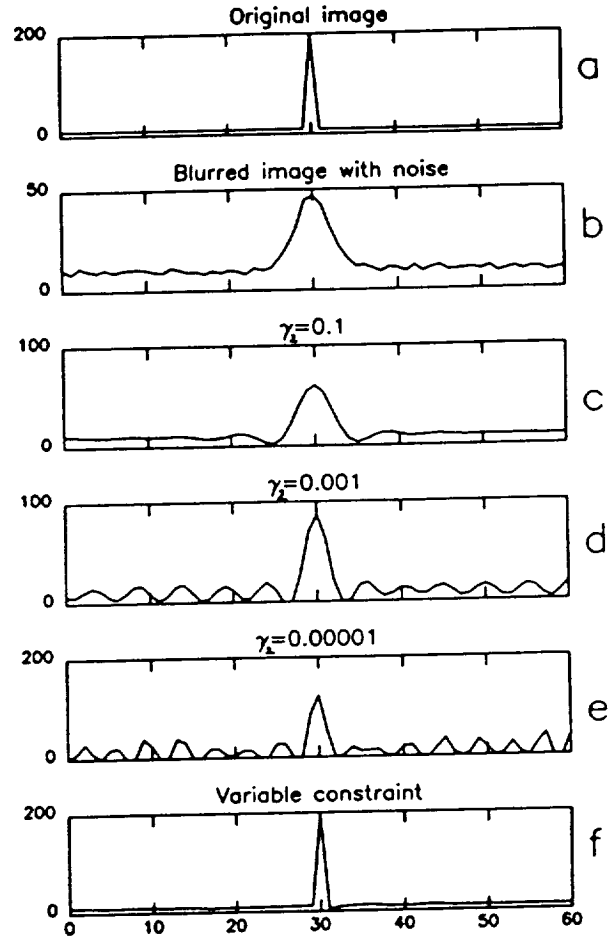

Figure 1. Effect of Langrangian multipliers. (a) original image;
(b) image blurred with a Gaussian PSF (σ=2.0 pixels) and noise added (σ=1 DN);
(c) restoration with γ_2=0.1;
(d) restoration with γ_2=0.001;
(e) restoration with γ_2=0.00001;
(f) restoration with γ_2=0.1 with constraint removed at the point source.

Multiple image constraints can be applied simultaneously:

$$\mathbf{x} = (H^T H + \gamma_a Q^T Q + \cdots + \gamma_t I)^{-1}(H^T \mathbf{b} + \gamma_t \mathbf{p}) \tag{7}$$

where a different value of γ can be selected for each constraint.

Selection of the reciprocal Lagragian multipliers can be done by visual inspection of the results for various values or by examination of the difference of blurred image and the solution re-convolved with the point spread function. This difference should have the same properties as the noise.

2.3 Missing or Bad Data Values

A problem occurs when trying to restore images with missing or bad data values (*i.e.* cosmic ray hits or bad CCD columns). If these defects are not taken into account in the restoration, their bad values will propagate to a larger portion of the output solution. (To some extent, every point in the solution depends on all values in the blurred image.)

One method of handling bad pixels is to attempt to repair them before restoration by interpolating from neighboring values. This approach is successful only if the repair is accurate. An alternative method is to make no attempt at prior repair but handle them in the restoration process. In this approach, the restored image will have more data values than the blurred image, and the linear system is underdetermined and, therefore, singular (*i.e.* no direct inverse exists). To ignore defective pixels, we set the corresponding rows in matrix H to zero.

This method of implementation (as opposed to removing row H creating a non-square underdetermined system) allows us to keep the matrix H square and decrease the complexity of implementation. Keeping H square in no way alleviates the problem of singularity. However, the method of constrained least squares solution does alleviate the problem of singularity and obtains reasonable solutions.

3. RESULTS

3.1 Ground Based image of QSO 2130+099

Although the first example is of a ground base image, it illustrates a case that may come up frequently with Hubble Space Telescope (HST) data. We have a bright point source on a lower level diffuse source. The wings of the bright source makes it difficult to study the underlying diffuse structure. One question, which may prove crucial to the understanding of the origin of QSO's, is: What kind of galaxy plays host to a QSO? The difficulty in answering this question is that the host galaxy appears as a faint fuzz around the bright QSO.

Our approach to deconvolve the QSO image is to make the assumption that the center of the galaxy contains a point source. As described in section 2.2, we use the method of constrained least-squares, apply two constraints simultaneously, one involving smoothness in the restored image (eq. 5), the other involving the deviation from a trial solution (eq. 6). The smoothness constraint is appropriate for the host galaxy and background sky. It is empatically not appropriate for the nucleus (QSO), since that by definition is a point-source. This is where
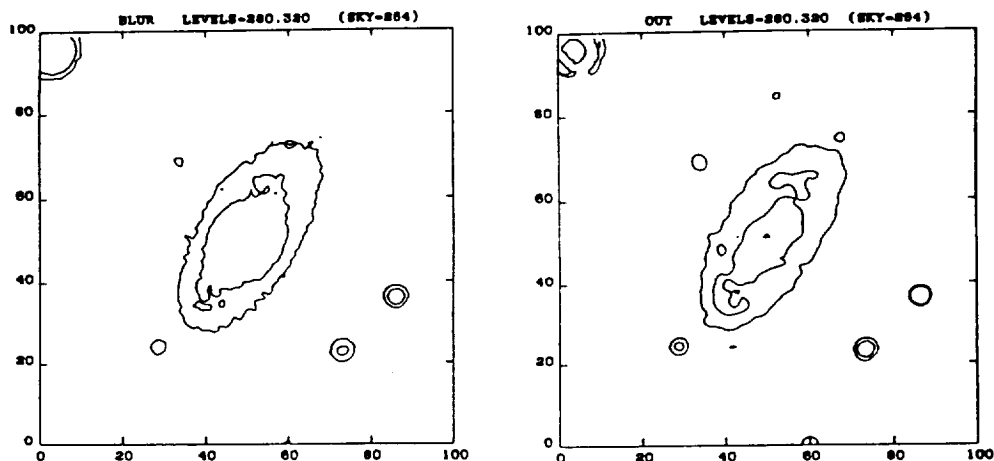
Figure 2. Contour plots of Quasar 2130+099. *Left*: the original image. The maximum count (at the nucleus of Q2130+099) is 21900 counts/pixel. *Right*: the restored image. The count level at the nucleus (the quasar) is now 324,000 counts/pixel. Both images have a plate scale of 0.6 arcsec per pixel; thus both span a 1' x 1' field. The two contour levels are at 280 and 320 counts per pixel; the average sky level is 254 counts/pixel.
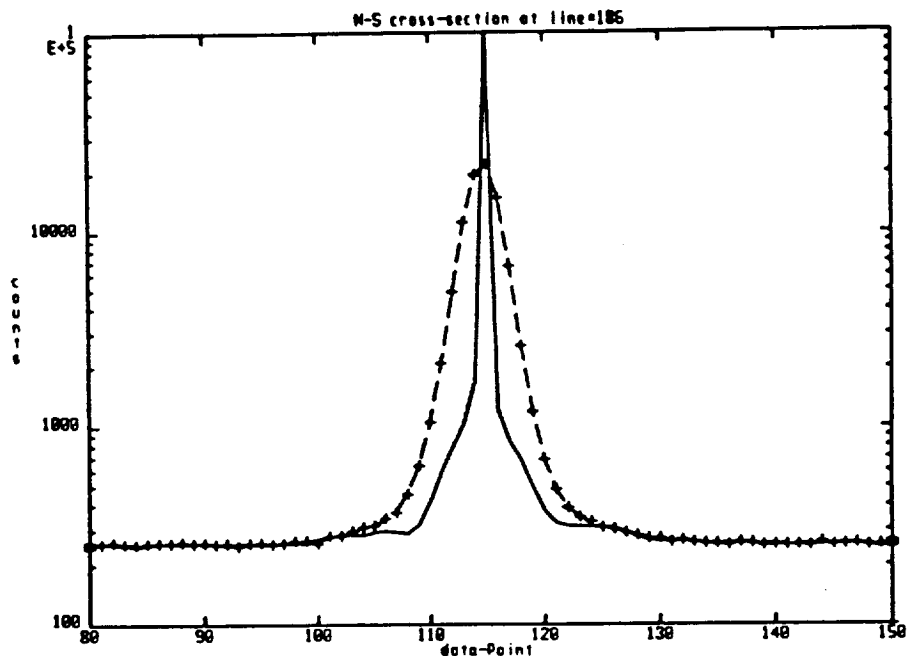
N-S cross-section at line=186

Figure 3. Cross-sectional plot of Q2130+099. The solid line shows the restored image. (The maximum count actually goes off-scale to 324,000 counts.) The pluses show the original (blurred image), while the dashed curve shows the result of convolving the restored image with the point-spread function.

the algebraic approach is so useful: it allows us to have local control of the constraints. We apply the smoothness constraint (minimize the Laplacian) and trial solution constraint (trial solution = sky background) to all the pixels in the image except the QSO.

Our example is a CCD image of QSO 2130+099 obtained by Tim Heckman at the 4-meter telescope at CTIO. QSO 2130+099, also known as II Zwicky 136, is a relatively nearby QSO with a redshift of only 0.06. Figure 2-left shows a contour plot ot the observed image at its lowest count levels. Not only can we see the galaxy extending 0.5 arcmin across the sky, but we can see two protrusions from the nucleus that look like spiral "stumps" if not full spiral arms. What we seek from deconvolution of Q2130+099 is not so much to enhance the resolution as it is to remove the veiling of the host galaxy by the QSO. Ideally, we would like to suck up all the flux from the QSO (nuclues) into a single pixel, so that we can look at what is around it. Figure 2-right shows the contour plot of the restored image at the same contour levels as before. Now the spiral arms arms are more prominent and fully devleloped.

Figure 3 shows a cross-sectional plot of the restored image. It shows Q2130+099 for what it is: an exceedingly bright nucleus (324,000 counts) embedded in a galxy whose surface brightness falls off exponentially with increasing distance from the center, a brightness distribution typical of spirals.

3.2 Wide Field Camera Image of R136

Figure 4-left shows a Wide Field Camera image of R136 in the Large Magellanic Cloud. It shows a crowded field of stars embedded in an underlying halo resulting from the wings of the HST point spread function. We could use the approach of the previous example: measuring the locations of all of the stars and applying a smoothness constraint at all locations except the star locations. This, however, would be difficult for very close stars and very dim stars which are difficult to see in the image. Errors in the stars' locations will result in a solution with artifacts. Another approach is to decrease the constraint at pixels with a higher probability of containing a star. A simple measure of the probability is the flux in the pixel. The larger the flux, the more probable that the pixel contains a star. In the solution, (figure 4-right) we have used a weighted constraint that minimizes the norm (sum of the squares) of the difference of the solution from zero. The weight at each pixel was selected as the log of its value in the previous iteration divided by its value in the previous iteration. As the solution converges the constraint converges to the minimization of:

$$\sum_i x_i log(x_i) \tag{8}$$

Note that the solution is no longer linear. Brighter stars are much sharper than dimmer stars. This can cause problems when performing photometry in the restored image. The accuracy of the photometry in the restored image is of major importance and will require additional investigation before we can make a reasonable assessment of the success of our restoration.
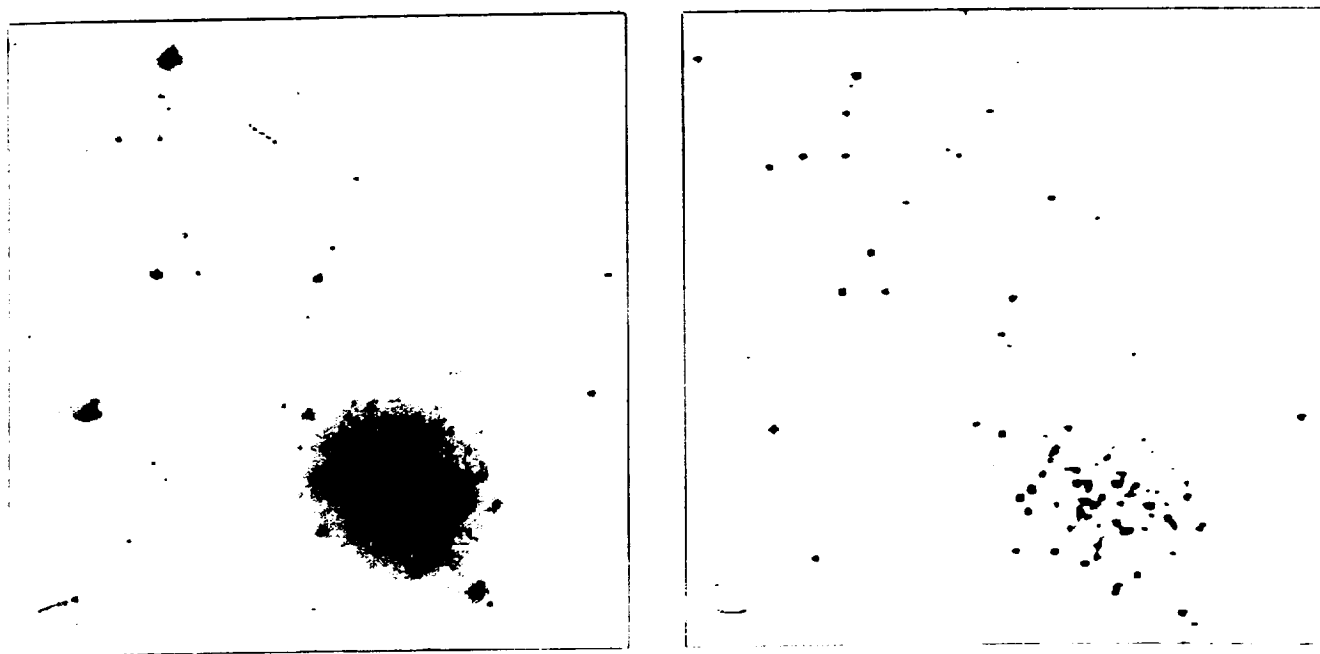
Figure 4: Restoration of Wide Field Camera image of R136

3.3 Wide Field Camera Images of Saturn

Figure 5 shows the restoration results for Wide Field Camera images of Saturn taken with three different wavelength filters. The images on the left are the unrestored, bias-subtracted and flat-fielded images. The images on the right show the results of the block iterative restoration algorithm using the minimization of the Laplacian ($\gamma_L=0.001$)and the minimization of the difference of each iteration from the previous iteration ($\gamma_t=0.01$) to constrain the solution. No attempt was made to repair bad pixels (e.g. cosmic rays) in the raw data. Instead, their locations were manually flagged and treated as missing data as described in section 2.3.

3.4 Goddard High Resolution Spectograph

The last example is a one-dimensional spectrum taken by the Goddard High Resolution Spectrograph (GHRS). The GHRS has two square science apertures: a 2.0 x 2.0 arcsecond Large Science Aperture (LSA) and a 0.25 x 0.25 arcsecond Small Science Aperture (SSA). The apertures have the feature that they cut off the wings of the HST point spread function at the edges of the apertures. The result is that the HST spherical aberration causes almost no loss of resolution when the SSA is used but does cause a significant loss of light. Only approximately 15 percent of the light from a point source centered in the SSA passes through the aperture.

Figure 5: Restorations (right) of bias subtracted and flat-fielded WFC images of Saturn. Top - filter F439W. Middle - filter F547M, Bottom - filter F718M
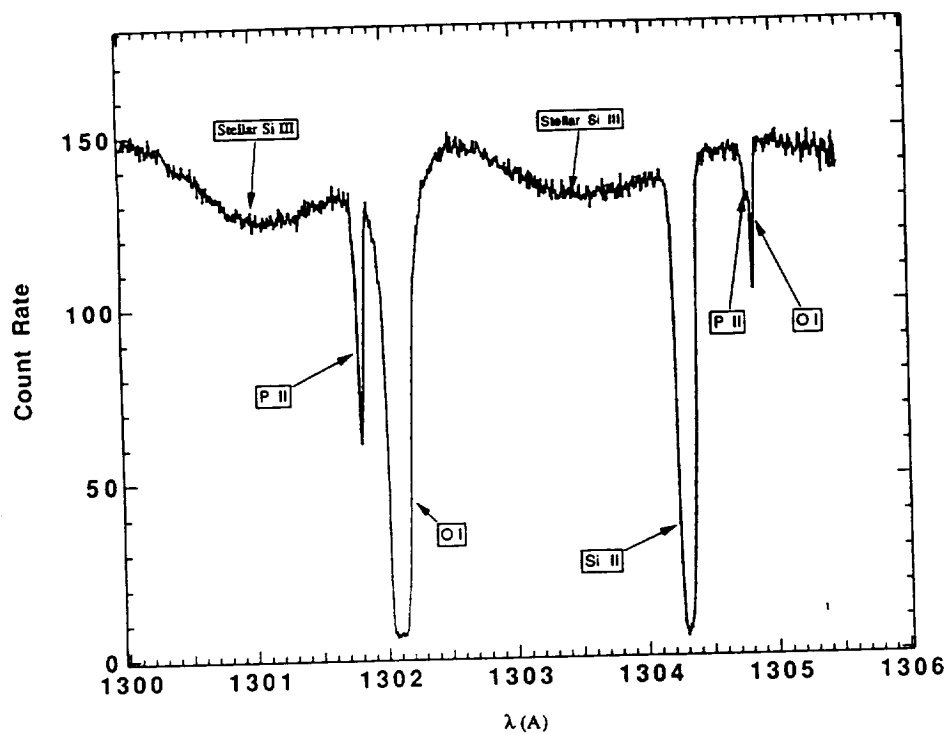
Figure 6: GHRS Large Science Aperture spectrum of ξ Persei
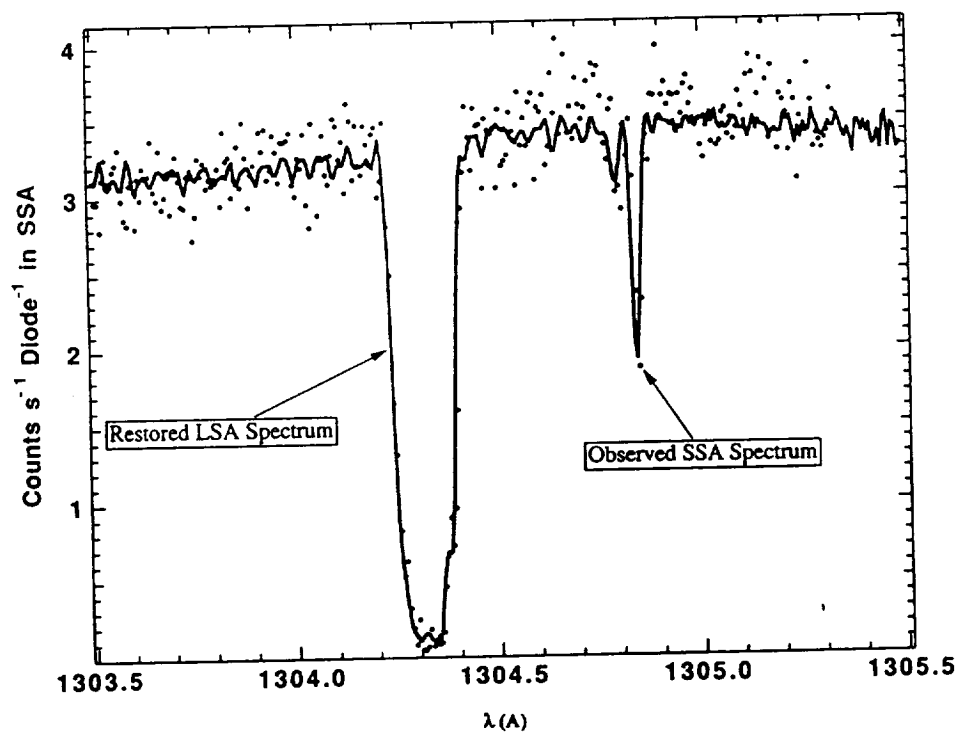

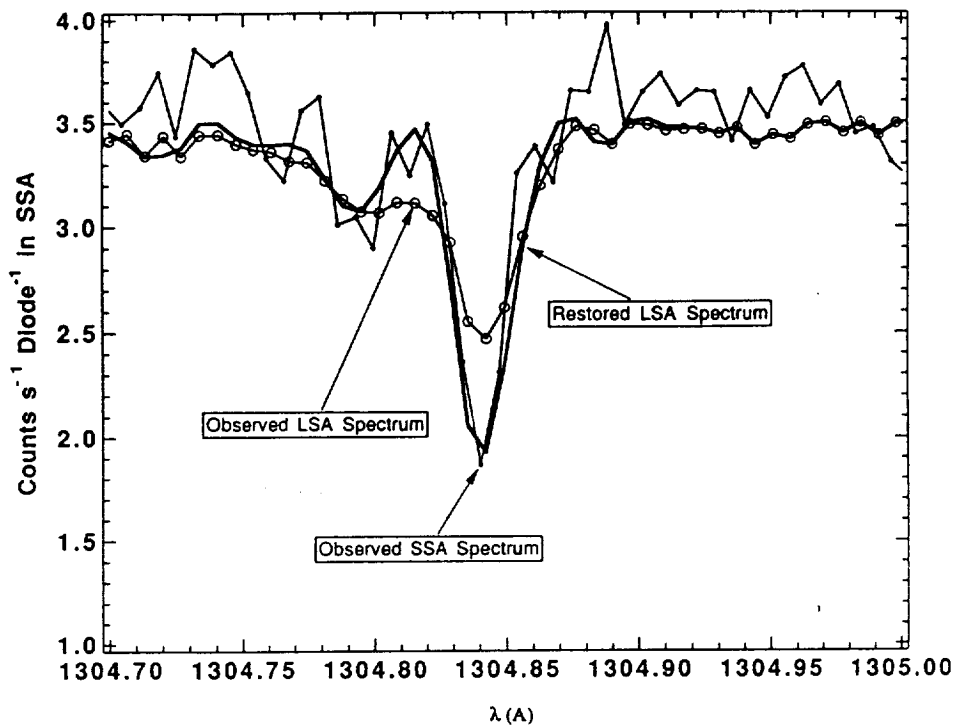Figure 7: Comparison of the restored LSA spectrum (solid line) with an observed SSA spectrum (dots)

Figure 8: Comparison of GHRS restored and unrestored LSA spectrum with a SSA spectrum

Approximately 60 percent of the light passes through the LSA at the cost of a significant amount of resolution.

A user of the GHRS must use the SSA (with a significant light loss) to obtain the best resolving power unless deconvolution of LSA spectra can recover the resolution of SSA spectra. Figure 6 shows a spectrum of ξ Persei observed through the LSA. Figure 7 shows the results of the block iterative restoration (solid line) compared to a SSA spectrum with a much smaller signal to noise (dots). Not only does the restoration separate the P II and O I lines at approximately 1304.8 angstroms (Also see figure 8) but it correctly restores the profile of the Si II line at 1304.3 angstroms.

REFERENCES

Andrews, H. C., Hunt, B. R. 1977, *Digital Image Restoration* (Prentice Hall: New Jersey), pp. 148-149.

Philips, D. L. 1962, "A Technique for the Numerical Solution of Certain Integral Equations of the First Kind", *J. ACM*, **9**, 84-97.

Twomey, S. 1963, "On the Numberical Solution of the Fredholm Integral Equations of the First Kind", *J. ACM*,**10**, 97-101 (1963).

Young, D. M. 1971, *Iterative Solution of Large Linear Systems*, (Academic Press: New York), pp. 434-437.